Three-Dimensional Analysis of Anisotropic Spatially Reinforced Structures

Alexander E. Bogdanovich

Latvian Academy of Sciences, Riga, Latvia
(Currently: Visiting Research Associate Professor, North Carolina State University
Raleigh, NC 27695-8301, USA)

SUMMARY

The material-adaptive three-dimensional analysis of inhomogeneous structures based on the meso-volume concept and application of deficient spline functions for displacement approximations is proposed. The general methodology is demonstrated on the example of a brick-type mosaic parallelepiped arbitrarily composed of anisotropic meso-volumes. A partition of each meso-volume into sub-elements, application of deficient spline functions for a local approximation of displacements and, finally, the use of the variational principle allows one to obtain displacements, strains and stresses at any point within the structural part. All of the necessary external and internal boundary conditions (including the conditions of continuity of transverse stresses at interfaces between adjacent meso-volumes) can be satisfied with requisite accuracy by increasing the density of tne sub-element mesh. The application of the methodology to textile composite materials is described. Several numerical examples for woven and braided rectangular composite plates and stiffened panels under transverse bending are considered. Some typical effects of stress concentrations due to the material inhomogeneities are demonstrated.

INTRODUCTION

Unlike traditional laminated materials, textile reinforced composites are characterized by a variation of their physical properties in all three directions. Therefore, textile composites have to be treated as complex three-dimensional hierarchical structures rather than as traditional, structurally quasi-homogeneous materials. However, the direct application of numerical analysis to a textile composite structural part starting with the hierarchical level "single fiber - matrix" seems to be unrealistic even when utilizing the most advanced super-computing facilities. Obviously, the analysis of a multi-level structured material has to be specified for the particular engineering problem.

For the case when only displacements are of interest, the analysis of a "fully homogenized" textile structural part may be useful in many practical situations. The whole part can thus be identified as a single "meso-volume" in the terminology of [1-3]. If the information about all six stress components in the structural part is needed, the internal interfaces gain importance and, correspondingly, the next hierarchical level has to be considered. At this level, the whole structure can be treated as an assemblage of distinct, anisotropic structurally homogeneous elements (meso-volumes). Starting at this level, some "global" failure effects in a structural part can be predicted using traditional phenomenological failure criteria. In the case when "local" failure effects are of interest, one has to start at the next hierarchical level, namely, the level of a single yarn surrounded by matrix material. The same concept of a meso-volume can be applied to this analysis supposing that a structurally homogeneous yarn element and matrix element represent two distinct types of meso-volumes [1]. Finally, the yarn itself can be considered as a complex structure. When the aim is predicting fracture initiation inside a single yarn, fiber elements surrounded by resin can be

considered as meso-volumes. Note that for traditional laminated composite structural parts there are three typical hierarchical levels: (i) an anisotropic homogenized structural part; (ii) an anisotropic structurally homogeneous layer; (iii) a single fiber surrounded by a matrix material. It is important to point out that the internal reinforcement architecture of textile composites at any of the sub-structural hierarchical levels is considerably more complex than reinforcement architecture of traditional laminated composites [4-7].

It follows from the above considerations that textile composite structures need a special approach for stress and failure analyses. Neither common theories of laminated structures with their corresponding finite element approaches nor strength-of-materials methodologies are usable.

In a "perfect" model of a composite laminate, as well as in a model for a spatially reinforced material, both the conditions of continuity of displacements and transverse stresses must be satisfied through the entire structural part. The continuity of transverse stresses can be achieved only if transverse strains are assumed to be discontinuous at each physical interface, as follows from Hooke's law. This leads to the requirement for the discontinuity of the first derivatives of displacements. Therefore, only those kinematic models which incorporate the above mentioned discontinuities can be considered valid. In [1] this topic was thoroughly discussed in the context of finite element modelling of laminated composite structures. According to the concept proposed, there is an opportunity to develop a rather general displacement-assumed computational model for a complex reinforced composite structural part using its primary "material-adaptive" partition into meso-volumes, then additional, purely computational partition into sub-elements inside each meso-volume. Afterwards, an approximation of the unknown displacement fields with respect to the whole discretization introduced by these two partitions in terms of deficient spline functions can be realized.

In the present paper this idea is used for the analysis of spatially reinforced rectangular plates and stiffened panels. To demonstrate the functionality of the method, several examples are considered. The first example models the behavior of a triaxially braided composite when the material is treated: (i) as a homogeneous material and (ii) as a six layer material. The structural responses predicted by modelling the material as an anisotropic homogeneous solid as opposed to a "laminate" are analyzed. The second example studies the behavior of a plain weave plate having geometrical parameters of the unit cell when modelled as a three-dimensional "brick" system. In the brick model presented herein, the material-adaptive aspect of the analysis is employed to maintain the continuity of displacements and stresses throughout the plate. Finally, a triaxially braided "skin - stiffener" structure is modelled using brick-type elements with elastic properties of distinct bricks derived from the homogenized properties of the triaxially braided material.

MATERIAL - ADAPTIVE ANALYSIS OF COMPOSITE STRUCTURES

Spline approximations

A general methodology for the analysis of inhomogeneous materials and structures can be demonstrated on the example of a brick-type mosaic parallelepiped shown in Figure 1, a. In this case the internal boundaries separate adjacent bricks (each brick having unique physical properties), and the boundaries are parallel to the side planes of the parallelepiped. Let us designate the set of planes containing all of these boundaries as $P_x=\{x=x_0=0,x=x_1,...,x=x_K=a\}$, $P_y=\{y=y_0=0,y=y_1,...,y=y_L=b\}$, and $P_z=\{z=z_0=0, z=z_1, ..., z=z_M=c\}$. Thus, the parallelepiped contains KxLxM structurally homogeneous meso-volumes. In general, each meso-volume has distinct properties, but in certain obvious practical situations some adjacent meso-volumes have identical properties. Accounting for this possibility is one of the key features of the algorithm to be developed.

A system of spline functions suitable for approximation of displacements in the parallelepiped must satisfy the following conditions:

(i) Spline functions dependent on each of the x, y, and z coordinates are continuous with respect to the corresponding coordinate inside the whole parallelepiped. This guarantees continuity of displacements inside the structurally inhomogeneous body;

(ii) At least one of the x- coordinate set of spline functions is characterized with discontinuous first derivative at each of the points $x=x_1$, $x=x_2$, ... , x_{k-1} where physical properties of adjacent meso-volumes are distinct. Analogous procedure is applied to the spline functions from the y- and z- coordinate sets. This is a necessary condition for satisfying the continuity of the corresponding transverse stresses (the detailed discussion on the problem of approximating functions can be found in [1]);

(iii) At any internal point of each meso-volume all of the approximating splines have the highest possible degree of continuity.

Construction of the approximation splines starts by generating another three sets of mutually parallel planes: $P_\xi = \{x=\xi_0=0, x=\xi_1, \dots, x=\xi_\lambda=a\}$, $P_\eta = \{y=\eta_0=0, y=\eta_1 \dots, y=\eta_\mu=b\}$, and $P_\zeta = \{z=\zeta_0=0, z=\zeta_1, \dots, z=\zeta_\nu=c\}$ that are of a purely computational meaning. The purpose of these planes is the same as for the sub-division planes introduced in [8] for a laminated plate, Figure 2. Note that all of the planes from the sets P_x, P_y, and P_z coincide with certain planes from the sets P_ξ, P_η, and P_ζ. The recursive procedure used here for derivation of the deficient splines of an arbitrary degree follows in its principal features the procedure worked out in [9], [10] for the case of second degree deficient splines.

The displacement field in the parallelepiped can be represented in the same form as for a laminated plate [8]:

$$u_x(x,y,z) = \sum_i \sum_j \sum_k U_{ijk}\, X_i^u(x)\, Y_j^u(y)\, Z_k^u(z)$$
$$u_y(x,y,z) = \sum_i \sum_j \sum_k V_{ijk}\, X_i^v(x)\, Y_j^v(y)\, Z_k^v(z) \qquad (1)$$
$$u_z(x,y,z) = \sum_i \sum_j \sum_k W_{ijk}\, X_i^w(x)\, Y_j^w(y)\, Z_k^w(z)$$

The difference appears only in the properties of the spline functions of the first and the second sets, namely $X_i^u(x)$, $X_i^v(x)$, $X_i^w(x)$ and $Y_j^u(y)$, $Y_j^v(y)$, $Y_j^w(y)$. They are not continuous like in the case of a laminated plate, but have selected discontinuous first derivatives.

Basic equations

The stress-strain equations for a generally anisotropic mosaic parallelepiped (Figure 1, a) can be written in the form

$$\begin{aligned}
\sigma_x &= Q_{11}(r)\,\varepsilon_x + Q_{12}(r)\,\varepsilon_y + Q_{13}(r)\,\varepsilon_z + Q_{14}(r)\,\gamma_{yz} + Q_{15}(r)\,\gamma_{xz} + Q_{16}(r)\,\gamma_{xy}\\
\sigma_y &= Q_{12}(r)\,\varepsilon_x + Q_{22}(r)\,\varepsilon_y + Q_{23}(r)\,\varepsilon_z + Q_{24}(r)\,\gamma_{yz} + Q_{25}(r)\,\gamma_{xz} + Q_{26}(r)\,\gamma_{xy}\\
\sigma_z &= Q_{13}(r)\,\varepsilon_x + Q_{23}(r)\,\varepsilon_y + Q_{33}(r)\,\varepsilon_z + Q_{34}(r)\,\gamma_{yz} + Q_{35}(r)\,\gamma_{xz} + Q_{36}(r)\,\gamma_{xy} \qquad (2)\\
\tau_{yz} &= Q_{14}(r)\,\varepsilon_x + Q_{24}(r)\,\varepsilon_y + Q_{34}(r)\,\varepsilon_z + Q_{44}(r)\,\gamma_{yz} + Q_{45}(r)\,\gamma_{xz} + Q_{46}(r)\,\gamma_{xy}\\
\tau_{xz} &= Q_{15}(r)\,\varepsilon_x + Q_{25}(r)\,\varepsilon_y + Q_{35}(r)\,\varepsilon_z + Q_{45}(r)\,\gamma_{yz} + Q_{55}(r)\,\gamma_{xz} + Q_{56}(r)\,\gamma_{xy}\\
\tau_{xy} &= Q_{16}(r)\,\varepsilon_x + Q_{26}(r)\,\varepsilon_y + Q_{36}(r)\,\varepsilon_z + Q_{46}(r)\,\gamma_{yz} + Q_{56}(r)\,\gamma_{xz} + Q_{66}(r)\,\gamma_{xy}
\end{aligned}$$

where $Q_{lm}(\mathbf{r})$ are step-wise functions of the position vector **r**. Then the linear strain-displacement equations are taken as:

$$\varepsilon_{xx} = \frac{\partial u_x}{\partial x}, \quad \varepsilon_{yy} = \frac{\partial u_y}{\partial y}, \quad \varepsilon_{zz} = \frac{\partial u_z}{\partial z}, \qquad (3)$$
$$\gamma_{xy} = \frac{\partial u_x}{\partial y} + \frac{\partial u_y}{\partial x}, \quad \gamma_{xz} = \frac{\partial u_x}{\partial z} + \frac{\partial u_z}{\partial x}, \quad \gamma_{yz} = \frac{\partial u_y}{\partial z} + \frac{\partial u_z}{\partial y}$$

The potential energy of the plate can be written as

$$P = \frac{1}{2} \int \int_V \int Q_{lm}(x, y, z)\, \varepsilon_l \varepsilon_m \, dx\, dy\, dz \qquad (4)$$

with l, m =1,..., 6; $\varepsilon_1 = \varepsilon_{xx}$, $\varepsilon_2 = \varepsilon_{yy}$, $\varepsilon_3 = \varepsilon_{zz}$, $\varepsilon_4 = \gamma_{yz}$, $\varepsilon_5 = \gamma_{xz}$, $\varepsilon_6 = \gamma_{xy}$.

The work of external force is expressed as follows

$$W = \int_S \int q(x, y)\, u_Z(x, y, h)\, dx\, dy \qquad (5)$$

where S is a loaded part of the surface z = h.

The solution procedure

The unknowns U_{ijk}, V_{ijk}, W_{ijk} can be calculated from the variational equation

$$\delta H = \delta(P - W) = 0 \qquad (6)$$

through the usual procedures.

It can be shown that the function H = P - W with the P and W defined accordingly to (4) and (5) can be written, after substitution of (1) and (2), (3), in the tensor form

$$H = (A_{ijklmn}\, U_{ijk}\, U_{lmn} + B_{ijklmn}\, V_{ijk}\, V_{lmn} + C_{ijklmn}\, W_{ijk}\, W_{lmn} + D_{ijklmn}\, U_{ijk}\, V_{lmn} + E_{ijklmn}\, U_{ijk}\, W_{lmn} + F_{ijklmn}\, V_{ijk}\, W_{lmn}) + (a_{ijk}\, U_{ijk} + b_{ijk}\, V_{ijk} + c_{ijk}\, W_{ijk}) \qquad (7)$$

where A_{ijklmn}, B_{ijklmn}, C_{ijklmn}, D_{ijklmn}, E_{ijklmn}, F_{ijklmn}, a_{ijk}, b_{ijk}, and c_{ijk} - unknown constants.

The first six of them depend on mechanical properties of the materials forming the parallelepiped while the other three depend on the surface and volumetric loads. The summation indices in (9) run: i and l from 1 to l_x, j and m from 1 to l_y, k and n from 1 to l_z. Here, $l_x = \lambda+1+K(m_x-1)$, $l_y = \mu+1+L(m_y-1)$, and $l_z = \nu+1+M(m_z-1)$.

The formulation of the solution procedure described above is not totally sufficient: it is applicable only if all of the meso-volumes have distinct properties. Hence, it does not allow one to correctly solve the particular case of the particular parallelepiped shown in Figure 1, a. For example, there is the surface element $\{x=x_2, y_0 \le y \le y_1, z_0 \le z \le z_1\}$ along which two identical meso-volumes interact. This means that the displacements here must have continuous first derivatives

C-4

with respect to x-coordinate. At the same time, this surface element belongs to the border between two meso-volumes and, according to the above procedure, the x-coordinate splines deficient at $x=x_2$ would be applied automatically (see Figure 1, b). Thus, the algorithm should be generalized in order to delete deficiencies along all surface elements separating distinct meso-volumes inside a mosaic parallelepiped. Mathematically it means that some constraints in the form of linear algebraic equations with respect to the unknown displacement coefficients U_{ijk}, V_{ijk}, and W_{ijk} are imposed on the original system of spline functions :

$$\alpha^p_{ijk} U_{ijk} + \beta^p_{ijk} V_{ijk} + \gamma^p_{ijk} W_{ijk} = \phi^p_{ijk} \tag{8}$$

where α^p_{ijk} , β^p_{ijk} , γ^p_{ijk} , and ϕ^p_{ijk} are predetermined constants, p is a number of constraints.

The procedure worked out for this purpose is illustrated graphically in Figure 1. At the first stage the original defects of the splines X_{s-1} and X_{s+1} at $x=x_2$(see Figure 1, b) are eliminated. The new system of splines is shown in Figure 1, c. Then, the defect of the spline X_s is eliminated, and the final system shown in Figure 1, d is obtained. It is easy to prove that this procedure is equivalent to the following constraint:

$$U_{s-1\,j\,k}\left(\frac{\partial X_{s-1}(x_2+0)}{\partial x} - \frac{\partial X_{s-1}(x_2-0)}{\partial x}\right) + U_{s\,j\,k}\left(\frac{\partial X_s(x_2+0)}{\partial x} - \frac{\partial X_s(x_2-0)}{\partial x}\right) + U_{s+1\,j\,k}\left(\frac{\partial X_{s+1}(x_2+0)}{\partial x} - \frac{\partial X_{s+1}(x_2-0)}{\partial x}\right) = 0 \tag{9}$$

Here, j and k run only the numbers corresponding to the splines of the sets $Y_j(y)$ and $Z_k(z)$ which have their supports inside the intervals $[y_0, y_1]$ and $[z_0, z_1]$ accordingly.

There is another problem with the construction of correct splines for the problem under consideration. In the particular case shown in Figure 1, a is a concern about the line segments $\{x=x_2, y=y_1, z_0 \le z \le z_1\}$ and $\{x=x_2, z=z_1, y_0 \le y \le y_1\}$ along which three different materials interact. For example, when moving to the second of these line segments in the vertical direction from the bottom ($z<z_1$) along any line $\{x=x_2, y=y^*\}$, $y_0 \le y^* \le y_1$, we have, under condition (9), that the displacements have continuous first derivatives with respect to x-coordinate. In the contrary, when moving to the same line segment from the top ($z>z_1$) along the line $\{x=x_2, y=y^*\}$, $y_0 \le y^* \le y_1$, we still have (and must have) displacements with discontinuous first derivatives with respect to x-coordinate. Therefore, at $z=z_1$ we have to satisfy the contradictory requests for the properties of $X_i(x)$ spline functions. It seems that this contradiction is of fundamental value and is related to the specific nature (possibly, singular behavior) of stress fields at the interactions of three different materials. This can not be principally improved in the current numerical approach, but can be localized in a small vicinity of the line segment using a partition of each meso-volume into sub-elements with three sets of planes P_ξ, P_η, and P_ζ. The effect of the named contradiction will be limited, for example, to the length of the support of the "transitional" spline $Z_t(z)$ (see, Figure 1, a).

The same form of constraints (8) can be used to specify the initial sets of approximating splines for some particular case of external boundary conditions at the edges of the mosaic parallelepiped. Formulation of various "global" and "local" edge boundary conditions in the context of the sub-layer/spline approximation method was discussed in [8, 11]. Clearly, the formulation of boundary conditions at the edges of a mosaic parallelepiped requires some additional discussion. However, we shall omit this discussion here, rather focusing only on some illustrative examples.

ANALYSIS OF TRIAXIALLY BRAIDED RECTANGULAR PLATES

In this study, a comparison is made for two models of a triaxially braided textile reinforced composite. The braid was modelled with a braiding angle of 63°, and the constituents were AS-4 carbon yarn as the reinforcement and Shell 1895 epoxy resin as the matrix.

The first model is based on a unit cell approach using a three dimensional representation of the reinforcing structure. The elastic properties of the unit cell were determined on the basis of a geometrical rendering of the reinforcement architecture. The geometrical rendering is illustrated in Figure 3. The stiffness matrix was determined by applying a Geometrically Integrated Numerical Analysis (GINA) technique [12]. Using this technique it is possible to evaluate the elastic properties of an arbitrary meso-volume. For the purposes of this analysis, the meso-volume was set to be the unit cell. The stiffness matrix predicted by this model is given below:

$$\mathbf{Q} = \begin{pmatrix} 56.46 & 17.68 & 8.88 & 0.004 & 0.058 & 1.299 \\ & 35.92 & 7.55 & -0.003 & 0.057 & 0.553 \\ & & 14.13 & 0.010 & 0.031 & 1.05 \\ & & & 12.99 & 0.206 & 0.055 \\ & \textit{sym} & & & 3.32 & 0.010 \\ & & & & & 4.13 \end{pmatrix} \text{ GPa} \qquad (10)$$

The second model provides a representation of the braided composite as a 6 layer symmetric angle-ply laminate. The ply lay-up assumed is $[63/0/-63°]_s$. The unidirectional (0°) layer properties were derived using the same fiber and resin materials properties as mentioned above through the micromechanics approach [10]. The properties of 63° and -63° layers were calculated from the properties of the 0° layer through the standard tensor transformation technique.

It should be pointed out that these two materials are not identical in terms of constituent ratios. The materials were modelled on the basis of realistic manufacturing processes. For the braiding system this assumed that the braider yarns were 12K, and the triaxial yarns were 24K tows. This results in 38.1% longitudinal yarns. In the case of the laminate, it was assumed that the plies each had the same thickness, thus 33% were longitudinals. The principal difference between these models is obvious: in the first model yarns have out-of-plane orientations, while the second model implies the in-plane reinforcement only. It is important to note that in the case of anisotropic, 3-D braided plate there is only one meso-volume within the plate which is identical, in its turn, to the unit cell, while the lamination model assumes 6 meso-volumes within the plate represented by distinct layers.

Numerical results were obtained for the square plate. The geometry parameters and the coordinate system used were taken the same as in the previous Section. Three combinations of the boundary conditions were considered:

ss-ss: at x=0 (s), at x=a (s), at y=0 (s), at y=a (s)
cc-ss: at x=0 (c), at x=a (c), at y=0 (s), at y=a (s) (11)
cs-ff: at x=0 (c), at x=a (s), at y=0 (f), at y=a (f)

where the following designation used: (s): $\sigma_x=u_y=u_z=0$ ($\sigma_y=u_x=u_z=0$) ; (c): $u_x=u_y=u_z=0$; (f): $\sigma_y=\tau_{xy}=\tau_{zy}=0$. The external load applied to the top surface z= h was prescribed by the equation

$$q = q_0 \sin\left(\pi \frac{x}{a}\right) \sin\left(\pi \frac{y}{b}\right) \qquad (12)$$

with a negative magnitude of q_0.

The symmetry of the solution can be used in the case of the boundary conditions "ss-ss" and a "braid" model only. In all the other cases full length and width of a plate have to be taken into consideration. The uniform divisions into 8 intervals in both x and y directions, as well as uniform divisions into 3 sub-layers of a homogeneous "braid" and each layer in a "laminate" were used. The third degree spline functions were employed.

Figure 4 shows the variation of σ_x as a function of x coordinate for y =0.5a, z=0. Figure 5 depicts the variation of σ_x throughout the thickness of a plate for x=0.5a and y=0.5a. Figure 6 demonstrates the dependency of $\tau_{xz}(z)$ for x=0.25a and y=0.25a.

From Figure 4, it is interesting to note that σ_x changes its sign along the length of the plate for the cases of boundary conditions "cc-cc" and "cs-ff". This stress component takes identical magnitudes for the values of $x \in [0.7a, a]$. This example demonstrates that for moderately thick anisotropic braided structure (with the aspect ratio a/h=10) the edge effect zones extend through its whole length.

Through-the-thickness distributions of both the stresses σ_x and τ_{xz} (Figures 5 and 6) are rather distinct for the "braid" and "laminate" models. The single-ply anisotropic material shows a smooth distribution, while for the 6-ply laminated material there are sharp "knees" at the ply interfaces. These results indicate that the structural response of a braided composite plate is influenced significantly by the number of meso-volumes representing the structure and the method used when modelling mechanical properties of a meso-volume.

APPLICATION OF THE THREE-DIMENSIONAL "BRICK" MODEL TO THE PLANE WEAVE RECTANGULAR PLATE

The meso-volume approach can also be applied to the unit cell problem to develop a picture of highly localized stress distributions associated with the cell. To examine the effectiveness of applying this approach, the plain weave unit cell shown in Figure 7 was modelled. The unit cell was divided into 32 meso-volumes (4 in x, 4 in y, and 2 in z) uniformly. Figure 7 illustrates the position of the meso-volumes within the unit cell, with sub-meso-volume divisions indicated by gray lines. Each meso-volume had distinct material properties. Figure 8 is a figurative representation of the Q_{11}, and Q_{22} values for the meso-volumes. There were no sub-divisions into sub-meso-volumes in the z direction. For both top and bottom, the meso-volumes A, D, M, and P (as well as A', D', M' and P') were divided into 9 sub-meso-volumes (3x3x1) nonuniformly. Meso-volumes B, C, E, H, I, L, N, and O were divided into 12 sub-meso-volumes (4x3x1 or 3x4x1). Meso-volumes F, G, J, and K were represented in terms of 16 sub-meso-volumes (4x4x1).

The structure was loaded sinusoidally, according to the equation (12), with a negative magnitude of q_0. The boundary conditions corresponded with simple support on all edges. The dimensions of the plate were a x b x h, with a/b = 0.75, and a/h = 24.

The most critical continuity concerns arise at the line of intersection of 4 distinct meso-volumes. Figure 9 illustrates the distribution of τ_{xz} as a function of z taken at two x values with y = 0.1875 b. The first case is x = 0.2499 a, and the second = 0.5001 a, which are just left and right of the interface between meso-volumes D-H, and D'-H'. It can be seen that the stress distribution for the two coordinates is extremely close.

Figure 10 examines the distribution of τ_{xy} as a function of x at the bottom surface (z=0). The first case is for y=0.2499 b, and the second for y=0.2501 b. This corresponds with lines running just beyond and just before the interfaces between meso-volumes A'-E', B'-F', C'-G', and D'-H'. In this case, the stress-concentrations associated with a material joint are revealed. This stress concentration can be considered a singularity contained within the border of sub-meso-volumes, but this has to be proved separately. By making the sub-meso-volume mesh denser in this region it is possible to localize the effect of this stress concentration within an arbitrary degree of precision. Beyond the stress concentration regions, the stress distributions on either side of the interface demonstrate continuity. This example shows that complex, structurally inhomogeneous parts can

be effectively analyzed by the numerical method presented in this paper, while satisfying all of the necessary continuity conditions.

APPLICATION OF THE THREE-DIMENSIONAL "BRICK" MODEL TO THE TRIAXIALLY BRAIDED SKIN-STIFFENER STRUCTURE

Problem formulation and solution procedure

Consider a rectangular laminated composite plate stiffened with a set of mutually parallel laminated composite beam elements having rectangular cross-sections (Figure 11). The stiffeners are, in general, non-equidistant. Geometric parameters and mechanical properties of any stiffener can be considered unique. A general type of anisotropic properties for a skin plate as well as for each of the stiffeners is assumed. It should be mentioned that another set of mutually parallel stiffeners (orthogonal to the first one) can be included without any changes in the analysis. For simplicity, only one set of stiffeners is shown in Figure 11.

In this analysis we shall focus on the skin-stiffener interaction problem. For this problem it is sufficient to analyze some representative element with its boundaries along the mid-lines between adjacent stiffeners (Figure 12). In general, the representative element can not be considered as a "unit cell" of a stiffened structure because of a distance variation between adjacent stiffeners as well as variations of an individual stiffener's characteristics. Nevertheless, the results obtained in the analysis of a single representative element should reveal all the main specific features of the interaction problem mentioned above.

Obviously, the analysis of stiffened panel element shown in Figure 13 can be developed in a direct way, by generalizing the analysis of [8]. Actually, this element is composed of the two 3-D anisotropic parallelepipeds (the skin and the stiffener). At the first step, both of them can be analyzed separately using the same approach [8]. At the second step, the specific boundary conditions imposed on displacements and transverse stresses at the interaction surface between these parallelepipeds must be satisfied, and the solution would be completed. When applying this approach, two distinct discretization meshes would possibly be used at the first stage assuming that the properties of the parallelepipeds are rather different. These meshes have to be chosen in order to satisfy the variational equation and all the external and internal boundary conditions for each of them [8]. The displacements and stresses obtained at the first stage still will contain some unknowns to be calculated from the continuity conditions at the interaction surface. This means that some functions referring to different meshes have to be matched. The described procedure, applied to all of the skin-stiffener interaction surfaces, may be cumbersome and computationally inefficient.

Another possible computational approach seems to be more elegant. By adding some fictitious "soft" material, the original, irregularly stiffened panel is completed up to the regular-shape parallelepiped (see Figure 11). Its thickness is equal to the total thickness of the skin and the highest stiffener. A filling material has to be chosen which will have no effect on the stress/strain state in the skin and stiffeners.

The "representative" element for this new structure can be extracted following Figures 12 and 13. This is an internally structured complex parallelepiped containing 3 different materials (the skin, the stiffener and the filler). Its structure can be characterized as a brick-type mosaic. The general "meso-volume" approach proposed in [1] can be applied to this type of structurally inhomogeneous material. In this particular case, the skin, the stiffener and the surrounding soft filler can be treated as three distinct meso-volumes. A unified discretization mesh can be introduced for the parallelepiped as a whole, and the appropriate system of 3-coordinate deficient spline functions has to be constructed for the analysis.

Orthotropic skin stiffened with an orthotropic stiffener

First consider a single-layer orthotropic plate stiffened with a single-layer orthotropic stiffener. Both the skin and the stiffener are made of the same carbon/epoxy unidirectionally reinforced composite material having the following elastic properties [13]:

$$E_1=25.0 \text{ Msi}, E_2=E_3=1.7 \text{ Msi}, G_{12}=G_{13}=G_{23}=0.65 \text{ Msi}, \nu_{12}=\nu_{13}=\nu_{23}=0.30. \quad (13)$$

For the skin the "1" direction goes along the x-axis; for the stiffener it goes along the y-axis. The fictitious "filler" is an isotropic material, its modulus E will be varied in magnitude, and Poisson's ratio is taken as 0.3.

Notations for the stiffened element are shown in Figure 13. The thickness of a skin h=a/20, the thickness of a stiffener h_s=a/20, and the width of a stiffener d=a/10. The element is under a sinusoidally distributed normal compressive load (12) applied to the top surface. In the following calculations it is taken a=b.

Due to the symmetry of a problem, a quarter of a stiffened panel, $0 \le x \le a/2$, $0 \le y \le b/2$ is solved. Boundary conditions at the side edges are:

$$\text{at } x=0: u_z = 0, u_y = 0, \sigma_x = 0; \quad (14)$$

$$\text{at } y=0: u_z = 0, u_x = 0, \sigma_y = 0. \quad (15)$$

Correspondingly, condition (15) is used at the stiffener's surface y=0.

The first task is to analyze an effect of a fictitious filler on a stress/strain state in the skin and the stiffener. The following partition of the skin, the stiffener and the filler is taken:

in x-direction: for any y and z values the interval [0, a/2-d/2] is divided uniformly into 6 parts, and the interval [a/2-d/2, a/2] is divided uniformly into 5 parts;

in y-direction: for any x and z values the interval [0, b/2] is divided uniformly into 4 parts;

in z-direction: for any x and y values both the intervals [0, h_s] and [h_s, c] are divided uniformly into 4 parts.

The distributions of σ_z, σ_x, and τ_{xz} along the x-coordinate at y=b/2, z=h_s are presented in Figure 14 for three magnitudes of the filler's elastic modulus: E/E_2 = 0.001 (case "a"), 0.01 (case "b"), and 0.1 (case "c"). A small difference between the curves "c" and "b" can be recognized, but the curves "b" and "a" absolutely coincide. The stresses σ_z and τ_{xz} are very close to zero at the main part of the free surface of the skin (z=h_s , $0 \le x \le 0.45a$). Small oscillations and non-zero values of σ_z and τ_{xz} in a vicinity of the point x=0.45a can be explained by the rather coarse x-direction mesh used in the analysis.

Another group of results for the same three magnitudes of E is presented in Figure 15. The dependencies $\sigma_x(z)$, $\tau_{xz}(z)$ at x=0.45a, y=0.5b as well as the dependency $\sigma_y(y)$ at x=0.45a, z=h_s/2 demonstrate the similar effect of the E magnitude as it results from Figure 7: there is some small difference in the curves for the cases "c" and "b", but no difference between the cases "b" and "a". As it is seen, the free surface condition for the stresses $\sigma_x(z)$ and $\tau_{xz}(z)$ at the side surface of the stiffener is fairly satisfied.

The results presented in Figures 14 and 15 lead to the conclusion that the value $E = 0.01E_2$ is sufficiently small. This value will be used in all of the following calculations.

It can be seen from Figures 14 and 15 that there are high stress gradients in the vicinity of the corner $x=0.45a$, $z=h_s$. The results obtained with the previous, rather coarse x-direction mesh are probably not accurate there. Convergence of stresses when increasing density of the mesh in x-direction has to be analyzed. In this analysis the above described meshes in y- and z-directions will be retained. The following node coordinates for the four meshes in x-direction will be used:

(i) $2x/a = 0.18, 0.36, 0.54, 0.72, 0.84, 0.87, 0.90, 0.93, 0.96, 0.98, 1.0$

(ii) $2x/a = 0.18, 0.36, 0.54, 0.72, 0.86, 0.88, 0.90, 0.92, 0.94, 0.96, 0.98, 1.0$

(iii) $2x/a = 0.18, 0.36, 0.54, 0.72, 0.868, 0.884, 0.900, 0.916, 0.932, 0.960, 0.980, 1.0$

(iv) $2x/a = 0.18, 0.36, 0.54, 0.72, 0.876, 0.888, 0.900, 0.912, 0.924, 0.960, 0.980, 1.0$

In each of these meshes there are two divisions to the left of the point $x=0.45a$ ($2x/a=0.9$) and two divisions to the right of this point having the same lengths, designated Δ. The value $2\Delta/d$ is equal to 0.3, 0.2, 0.16, and 0.12 for the meshes (i)-(iv) correspondingly.

The dependencies of σ_z, τ_{xz}, σ_x, and σ_y on $2\Delta/d$ at the corner point $x=0.45a$, $y=0.5b$, $z=h_s$ are presented in Figure 16. It looks like there are no finite limits of σ_z, τ_{xz}, and σ_y with Δ going to zero. This indicates, probably, a singular behavior of these functions along the line $x=0.45a$, $z=h_s$. On the contrary, σ_x does not depend on Δ. This reasonable result encourages the belief that the tendencies shown by the other three curves have some physical meaning. Note also that σ_z is tensile, and σ_x considerably exceeds the other three stresses. Undoubtedly, the effects revealed ask for a more detailed analysis.

The next issue of a certain interest is the behavior of contact stresses σ_z, τ_{xz}, and τ_{yz} at the skin-stiffener interaction area. They were calculated with the same y- and z- meshes as before and with the following three x-meshes:

(I) uniform for both the skin and the stiffener; each of the intervals [0, 0.45a] and [0.45a, 0.5a] is divided into 9 parts;

(II) $2x/a = 0.15, 0.30, 0.45, 0.60, 0.70, 0.825, 0.850, 0.875, 0.900, 0.911, 0.922, 0.933, 0.944, 0.955, 0.966, 0.977, 0.988, 1.0.$

(III) $2x/a = 0.15, 0.30, 0.45, 0.60, 0.80, 0.87, 0.88, 0.89, 0.90, 0.911, 0.922, 0.933, 0.944, 0.955, 0.966, 0.977, 0.988, 1.0.$

Distributions of σ_z, τ_{xz}, and τ_{yz} along the half-width of the stiffener at $z=h_s$, $y=0.5b$ (for σ_x and τ_{xz}) and $y=0.25b$ (for τ_{xy}) are presented in Figure 17. For any of these stresses, the three curves corresponding to the mesh (I) and the meshes (II) and (III) are distinct only inside a small x interval adjacent to the corner $x=0.45a$, $z=h_s$ where the contact stresses increase sharply. However, even near this corner the curves corresponding to the meshes (II) and (III) coincide. Note that the normal contact stress σ_z changes its sign and becomes tensile at $x<0.458a$. These results demonstrate that the realistic distributions of contact stresses in the problem of skin-stiffener interaction are very complex. Definitely, they would play a major role in the predictions of failure initiation in stiffened structures.

Triaxially braided T-section plate

A structural element of the same type as in Figure 13 is considered here. It is made of a triaxially braided composite characterized with the stiffness matrix (10). The element is modelled with both version "a" and version "b" brick-type mosaic structures shown in Figure 18. In both cases the meso-volume "A" has the stiffness (10) with material axes 1, 2, and 3 going along the plate axes x, y, and z correspondingly. The meso-volume "B" is characterized with the same stiffness matrix, but the material axes 1 and 3 correspond to the plate axes z and x in this case. Still, axis 2 goes along with axis y. All the other meso-volumes involved in the analysis, namely, C, D, E, and C', C", D', D", E', E", have their stiffness matrices generated from the matrix (10) as something intermediate between the matrices for the meso-volumes "A" and "B". The purpose of these intermediate meso-volumes is to provide a smooth transition inside the zone between meso-volumes "A" and "B". It is assumed that all of them have distinct elastic characteristics.

The element shown in Figure 18 is loaded with a sinusoidally distributed surface pressure (12) (see Figure 13). All four side edges are assumed to be simply supported. The full length of the plate is a=100, its full width b=200, and the skin stiffness h=10. The stiffener width is d=20 and its thickness h_s=40. Due to the symmetry, one quarter of the element was solved. The numerical results obtained for the element divisions into meso-volumes, cases "a" and "b", are presented in Figures 19-25.

As can be seen in Figure 19, the distribution of σ_z along z inside the skin and stiffener is a smooth curve with a maximum on the skin-stiffener contact point. There is no difference between the variants "a" and "b". On the contrary, the distribution of the same stress along z at the stiffener's side surface (Figure 20) has a pronounced spike at the corner x=0.4a, z=z_s. Note that in this case the maximum of σ_z is tensile. The same character of distributions can be seen for τ_{xz} in Figure 21 and for σ_x in Figure 22. There is an almost negligible difference between the variants "a" and "b".

The distributions of σ_x and τ_{xz} along the x coordinate presented in Figures 23 and 24 show again sharp spikes around the corner of the skin and the stiffener. Finally, the monotonic curve shown in Figure 25 characterizes the distribution of σ_y on y coordinate inside the skin and the stiffener.

The stress fields σ_z and σ_x along the plane z=40 are shown in Figures 26 and 27. They clearly demonstrate a high stress concentration around the skin-stiffener contact area.

The problem treated in this Section is very complex. The results presented can be considered as preliminary. A detailed convergence analysis when using finer meso-volumes as well as sub-meso-volume meshes is needed. It can be expected from the results above that there are singularities of some stress components at the corner x=0.4a, z=z_s. Still, to the author's best knowledge there are no other formulations and solutions for the class of problems addressed in this paper.

CONCLUSIONS

The sub-layer/spline approximation method developed in the previous works for a 3-D analysis of laminated plates has been generalized in this work for the solution of 3-D elasticity problems for a brick-type mosaic structure. The material-adaptive approximation of displacements with deficient spline-functions is used. It allows one to eliminate, or at least localize, the unwanted jumps of transverse stresses at the interfaces. The development of internal continuity conditions depend on the physical description of the structural part, and is specifically constructed for inhomogeneous structural materials (laminates, 3-D woven, triaxially braided, and 2-D woven composites). Calculation of material properties of each meso-volume are based upon the geometry of the actual material. Incorporating the geometric description of the reinforcement into the structural analysis

yields a precise and complete theoretical description of the material without depending upon data from other sources, which may not be available.

A representative element of a stiffened laminated or textile-reinforced composite panel can be considered as a particular case of a brick-type mosaic parallelepiped. In order to use this approach in the analysis, a fictitious "soft" material was added to the stiffened panel. The procedure of developing the correct spline approximation functions for this problem was discussed. The stress concentrations at the contact zone between the stiffener and the skin have been investigated for the "orthotropic skin-orthotropic stiffener" structure. It was found that the spike values of σ_z, τ_{xz}, and σ_y stresses do not converge when increasing mesh density. This indicates that singularities can be expected at the contact zone.

The analysis carried out for the T-profile triaxially braided plate revealed high stress concentrations around the corner. This zone has to be considered as the most suspicious for the failure initiation. It was shown also that the stress concentrations are sensitive to the number of meso-volumes used in the representation of a "transitional zone".

The method has been shown to be successful in analyzing three different types of textile composite structures. With this tool there are many problems that can be addressed which have not been solved previously.

ACKNOWLEDGEMENTS

The author wishes to extend thanks to Dr. Christopher M. Pastore who provided the mechanical characteristics of braided and woven materials used in the numerical examples, and to Mr. Alexander Birger who coded the structural analysis program and carried out the computational work.

The author would like to acknowledge the North Carolina Supercomputing Association for use of their super-computing facilities in the solution of the numerical problems.

REFERENCES

1. Bogdanovich, A. E. : Spline Function Aided Analysis of Inhomogeneous Materials and Structures. Proceedings of the IUTAM Symposium "Local Mechanics Concepts for Composite Material Systems", Blacksburg, Virginia, USA, October 28-31, 1991. Berlin-Heidelberg-New York: Springer-Werlag, J. N. Reddy, K. L. Reifsnider (Eds.), 1992, pp. 355-382.

2. Bogdanovich, A. E. ; Pastore, C. M. : On the Structural Analysis of Textile Composites. Topics on Composite Materials and Structures, AE - vol. 26, AMD - vol. 133, ASME Publications, 1992, pp. 13-19.

3. Pastore, C. M. ; Bogdanovich, A. E. ; and Gowayed, Y. A. : Applications of a Meso-Volume-Based Analysis for Textile Composite Structures. Composites Engineering, vol. 3, no. 2, 1993, pp. 181-194.

4. Tarnopol'skii, Yu. M. ; Zhigun, I. G. ; and Polyakov, V. A. : Spatially Reinforced Composite Materials. Moscow, Mashinostrojenije Publishers, 1987 (in Russian). English translation by Technomic Publishers, 1992.

5. Chou, T. W. ; and Ko, F. K. : Textile Structural Composites. Elsevier, Essex, UK, 1988.

6. Ko, Frank K. : Preform Fiber Architecture for Ceramic - Matrix Composites. American Ceramic Society Bulletin, vol. 68, no. 2, February 1989, pp. 401-414.

7. Tan, T. M. ; Pastore, C. M. ; and Ko, F. K. : Engineering Design of Tough Ceramic Matrix Composites for Turbine Components. Journal of Engineering for Gas Turbines and Power, vol. 113, no. 2, April 1991, pp. 312-317.

8. Bogdanovich, A. E. ; and Birger, A. B. : Application of Spline Functions to the 3-D Analysis of Laminated Composite Plates Subject to Static Bending. Proceedings of the Second International Symposium on Composite Materials and Structures, Beijing, China, August 2-5, 1992. Peking University Press, pp. 719-725.

9. Bogdanovich, A. E. ; and Yarve, E. V. : Numerical Solution of a Two-Dimensional Problem of Nonsteady Deformation of Laminated Media. Mechanics of Composite Materials (in Russian), translated by Consultants Bureau. New York: Plenum Publishing Corporation, no. 1, 1988, pp. 31-38.

10. Bogdanovich, A. E. ; and Iarve, E. V. : Numerical Analysis of Impact Deformation and Failure in Composite Plates. Journal of Composite Materials, vol. 26, no. 4, 1992, pp. 520-545.

11. Bogdanovich, A. E. ; and Birger, A. B. : Application of Spline Functions to the Analysis of Local Boundary Effects in Laminated Composite Plates. To be published in Proceedings of the ASME Winter Annual Meeting, Anaheim, California, November 8-13, 1992.

12. Gowayed, Y.A. : An integrated approach to the mechanical and geometrical modelling textile structural composites. Ph.D. Thesis, North Carolina State University, Raleigh, N.C. USA, 1992.

13. Humpreys, E. A. ; and Rosen, B. W. : Properties Analysis of Laminates. Engineering Materials Handbook, vol. 1. Composites. ASM International, 1987, p. 223.

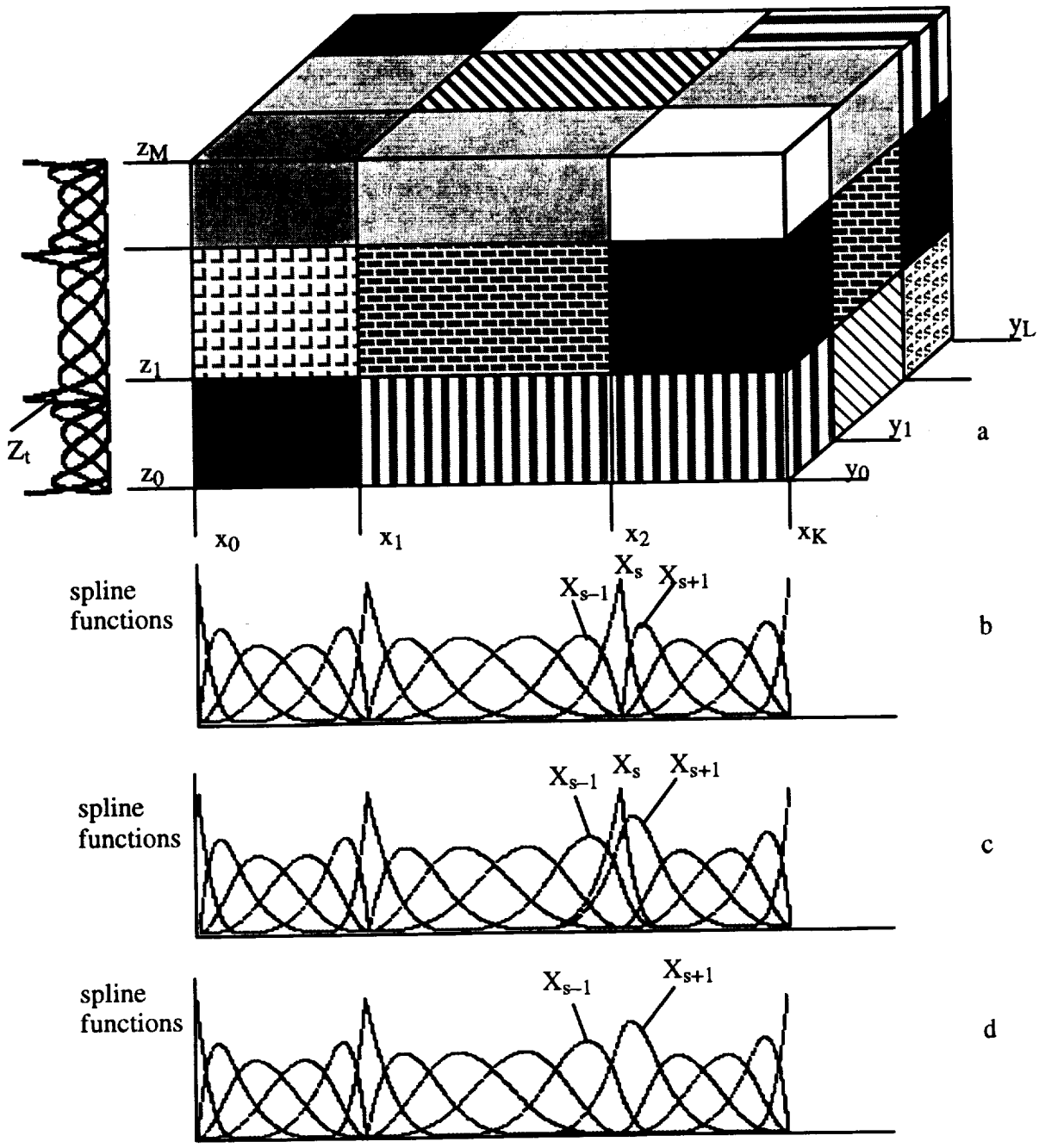

Figure 1. Brick–type mosaic parallelepiped (a) and illustration of the procedure used for removing the defect at the surface $x=x_2$, $y_0 \leq y \leq y_1$, $z_0 \leq z \leq z_1$ (b,c,d).

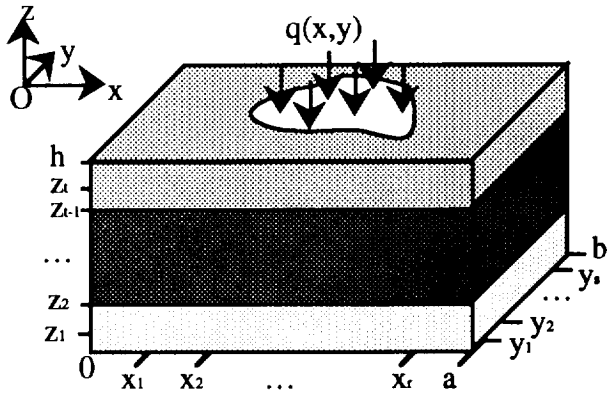

Figure 2. Notations used in a plate analysis.

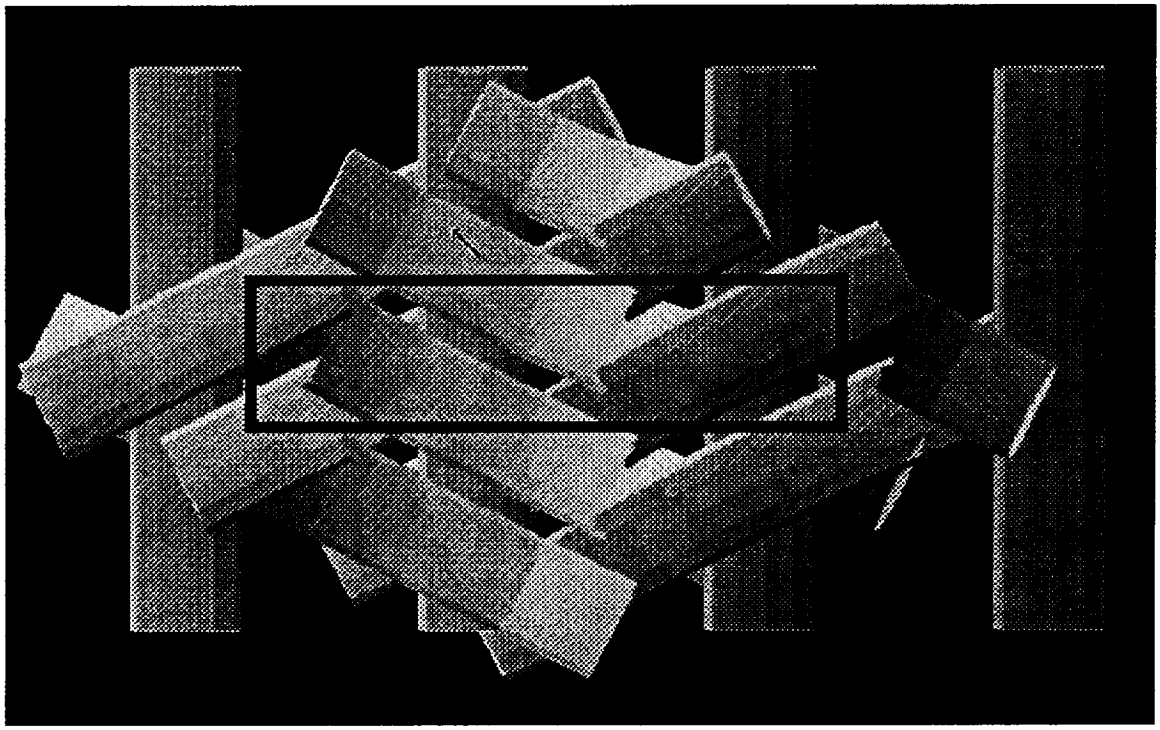

Figure 3. Schematic Illustration of Triaxially Braided Fabric Structure Showing Unit Cell Dimensions Used for Calculation.

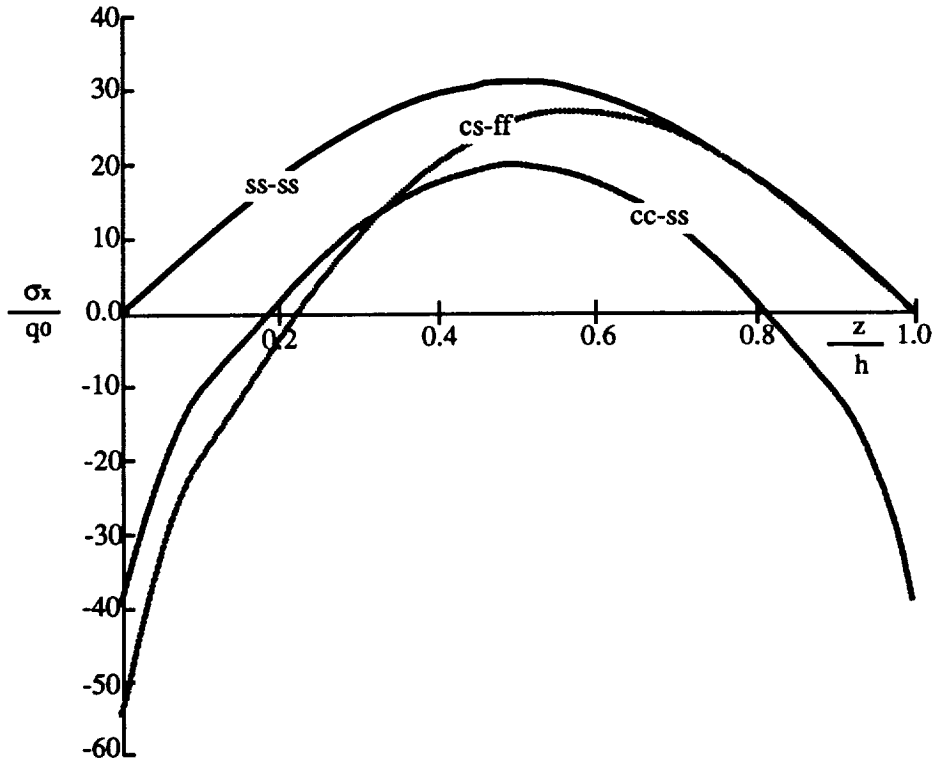

Figure 4. Variation of σ_x as a function of length coordinate for the "braid" model under three combinations of boundary conditions.

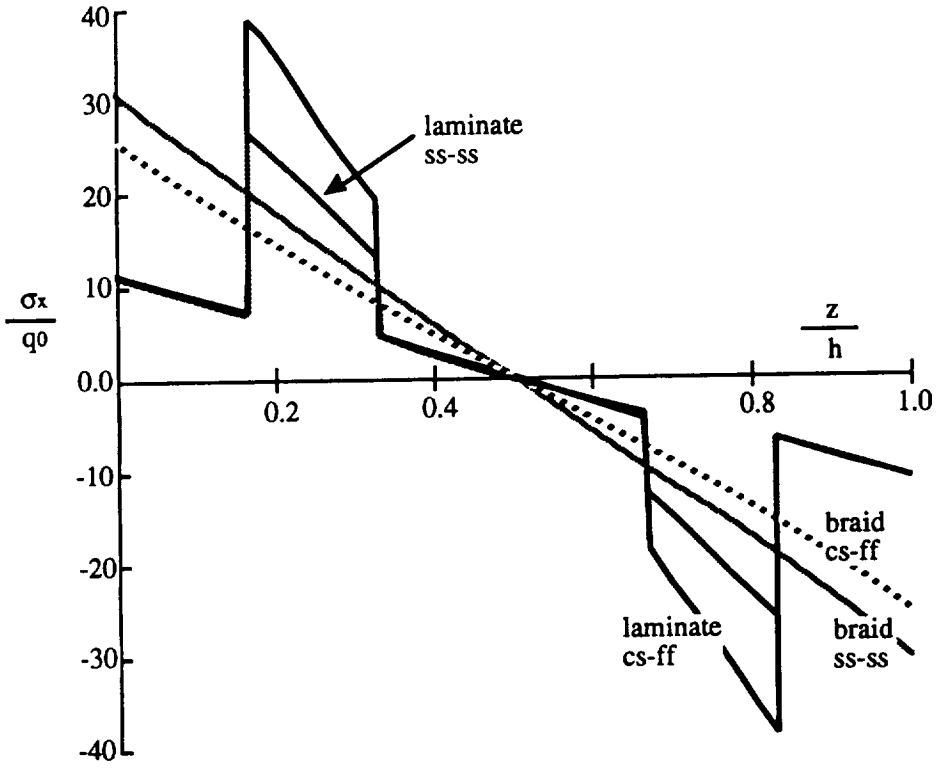

Figure 5. Variation of σ_x as a function of length coordinate for "laminate" and " braid" models under two combinations of boundary conditions.

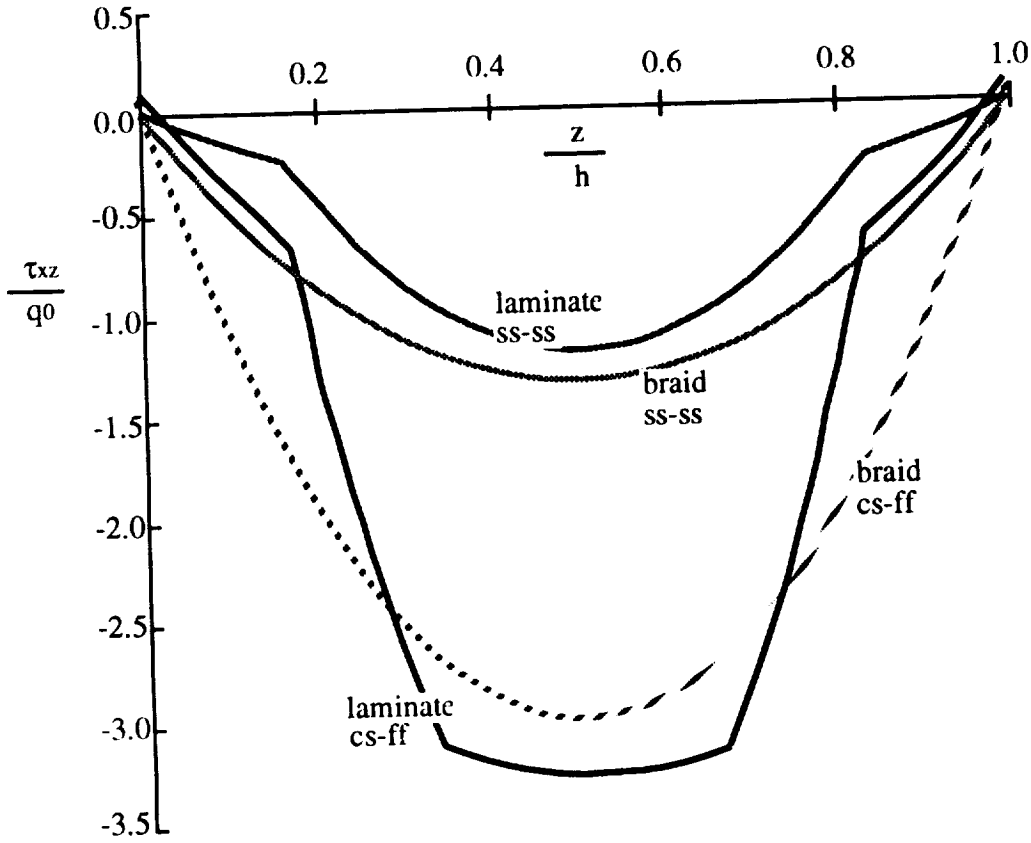

Figure 6. Variation of τ_{xz} as a function of thickness coordinate for "laminate" and "braid" under two combinations of boundary conditions.

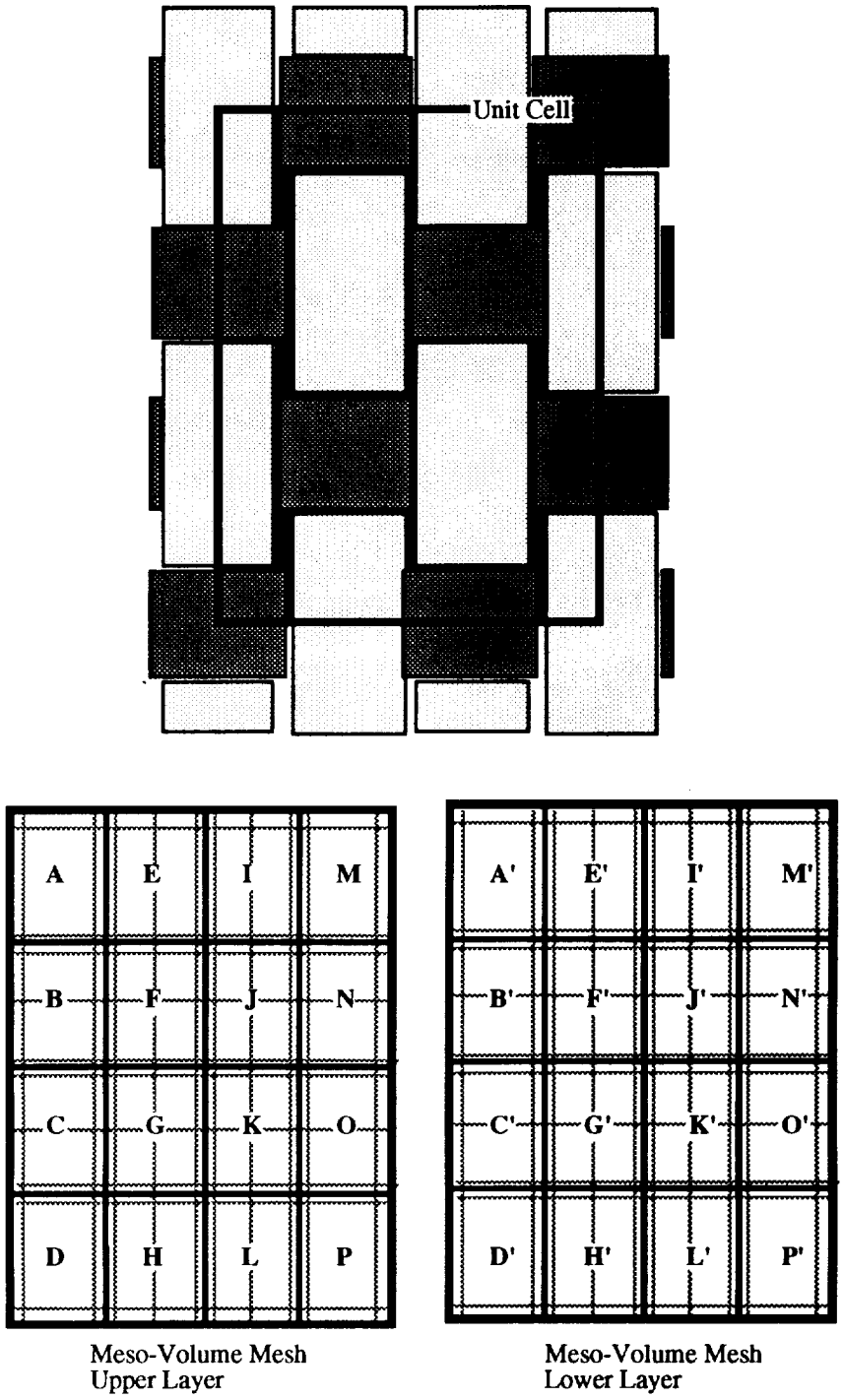

Figure 7. Schematic Illustration of Weave Unit Cell and the Meso-Volume Mesh.

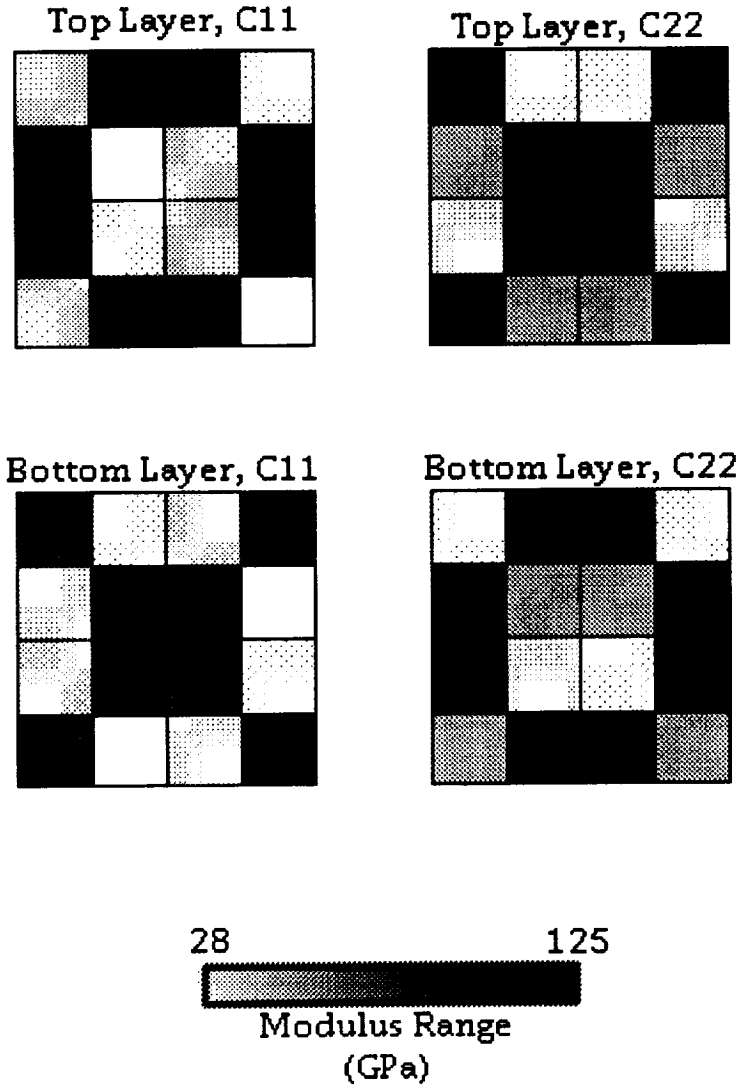

Figure 8. Schematic Drawing Showing Q_{11} and Q_{22} Values Associated with the Meso-Volumes for the Plain Weave Brick Model.

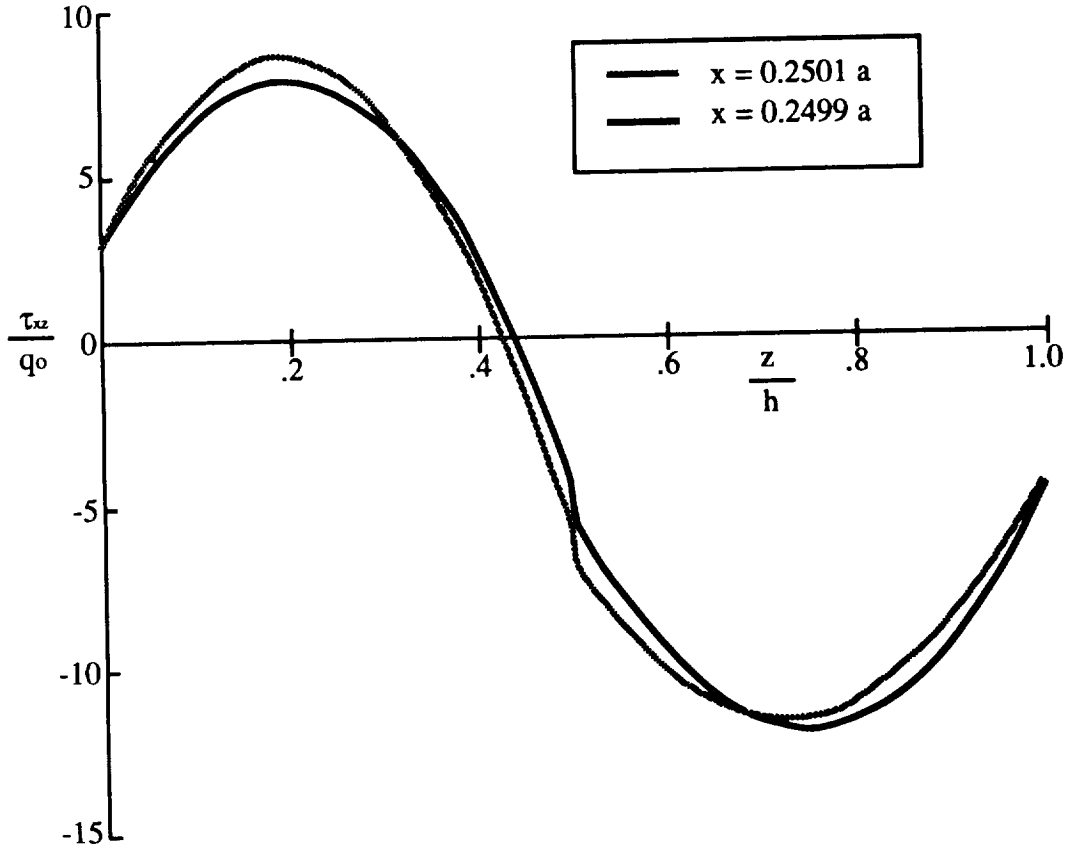

Figure 9. Distribution of τ_{xz} as a function of z, for y = 0.1875 b, at the lines on either side of the meso-volume interface.

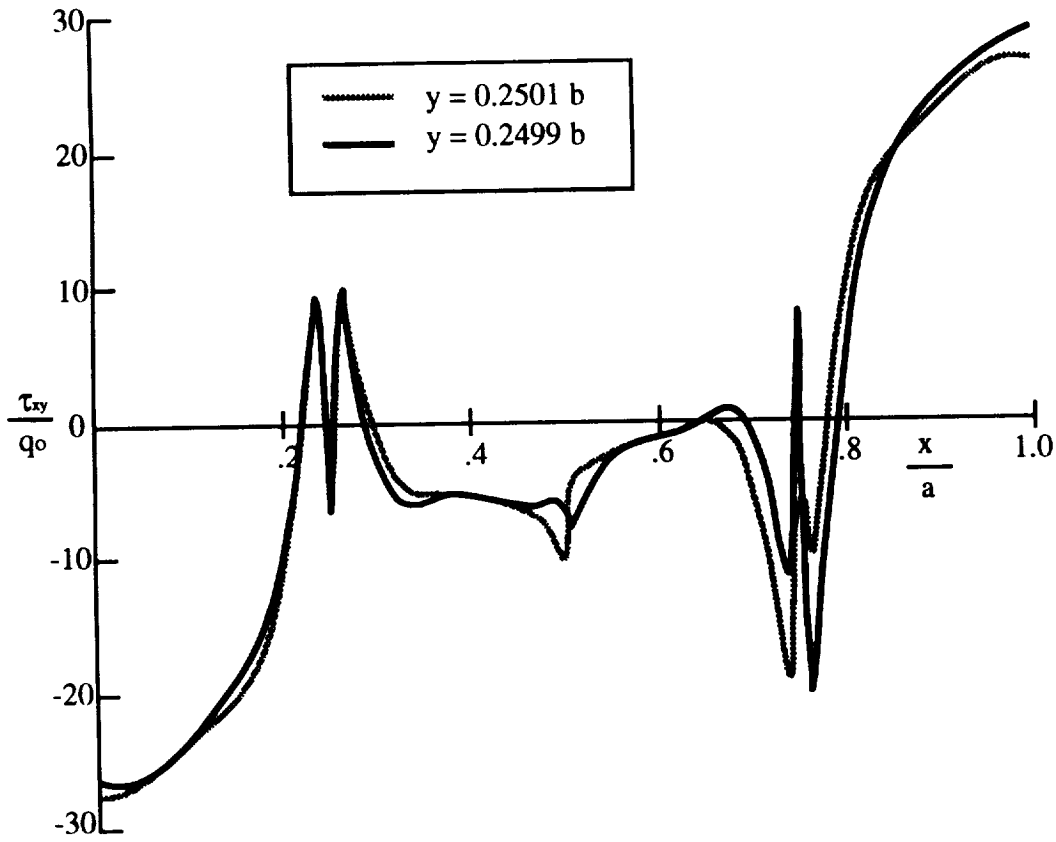

Figure 10. Distribution of τ_{xy} as a function of x, for z = 0, at the lines on either side of the meso-volume interface.

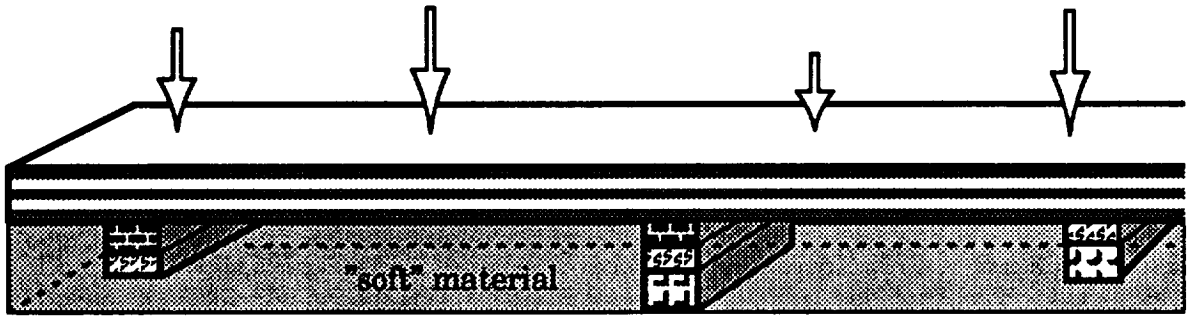

Figure 11. Stiffened composite panel structure filled with a "soft" material.

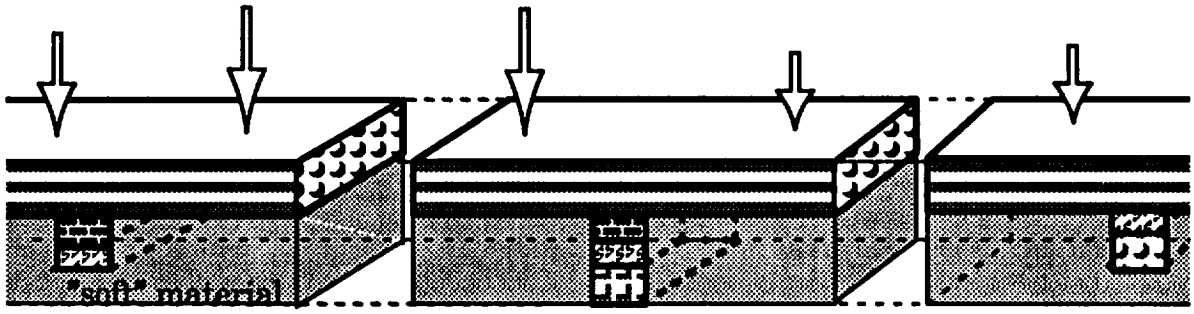

Figure 12. Division of the filled panel into representative elements.

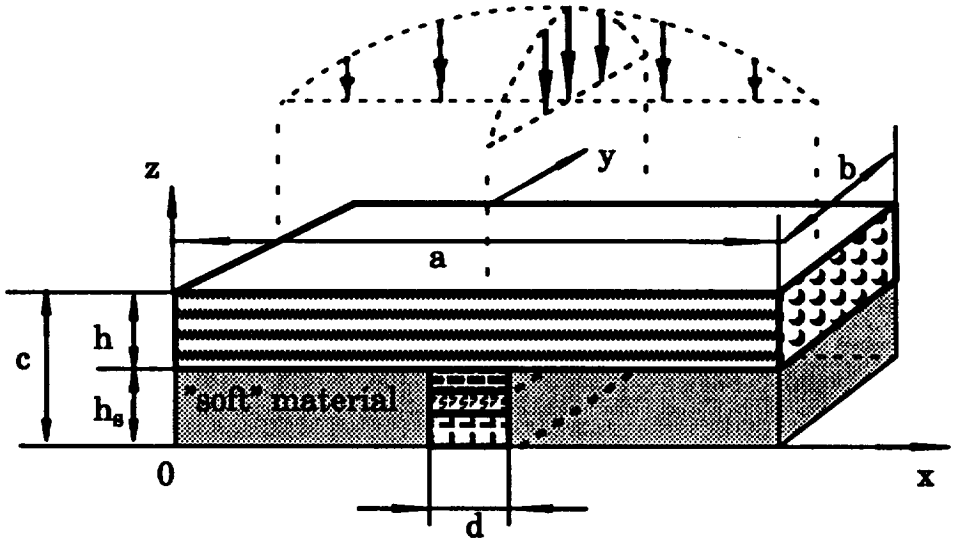

Figure 13. Notation used for the representative element.

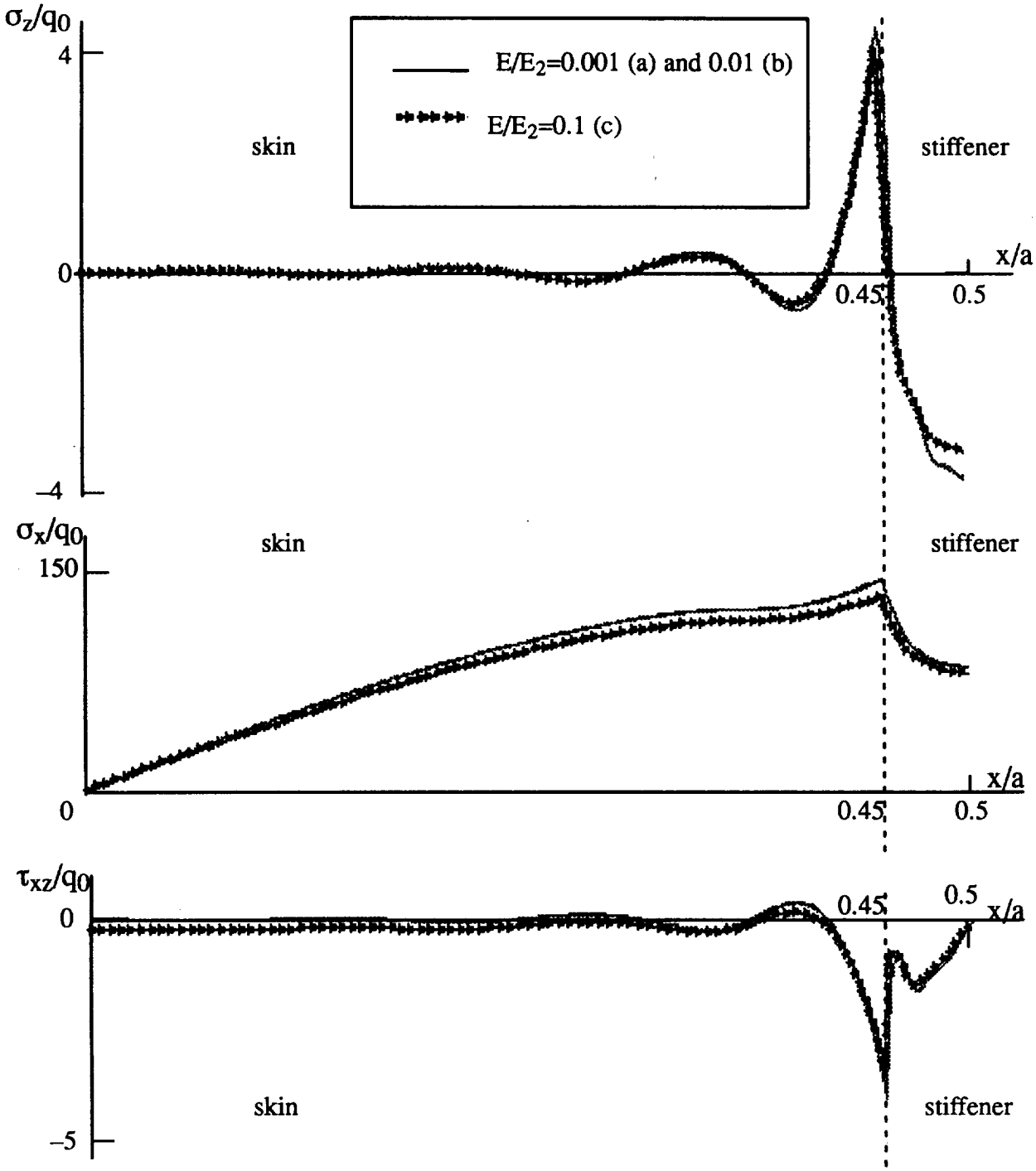

Figure 14. Variations of σ_z, σ_x, and τ_{xz} along x–coordinate for three magnitudes of the filler's modulus E.

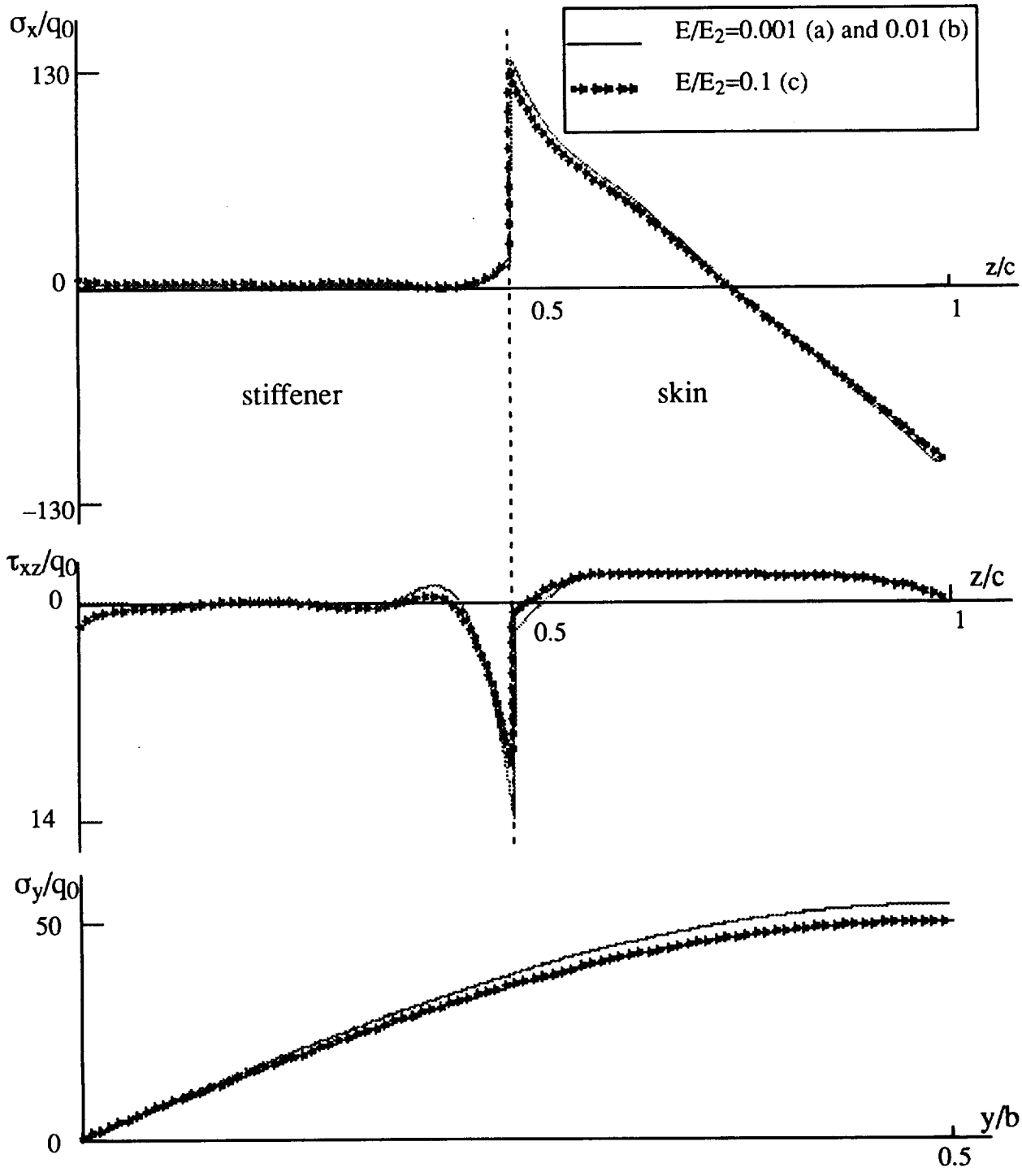

Figure 15. Variations of σ_x, τ_{xz} along z–coordinate and σ_y along y–coordinate for three magnitudes of the filler's modulus E.

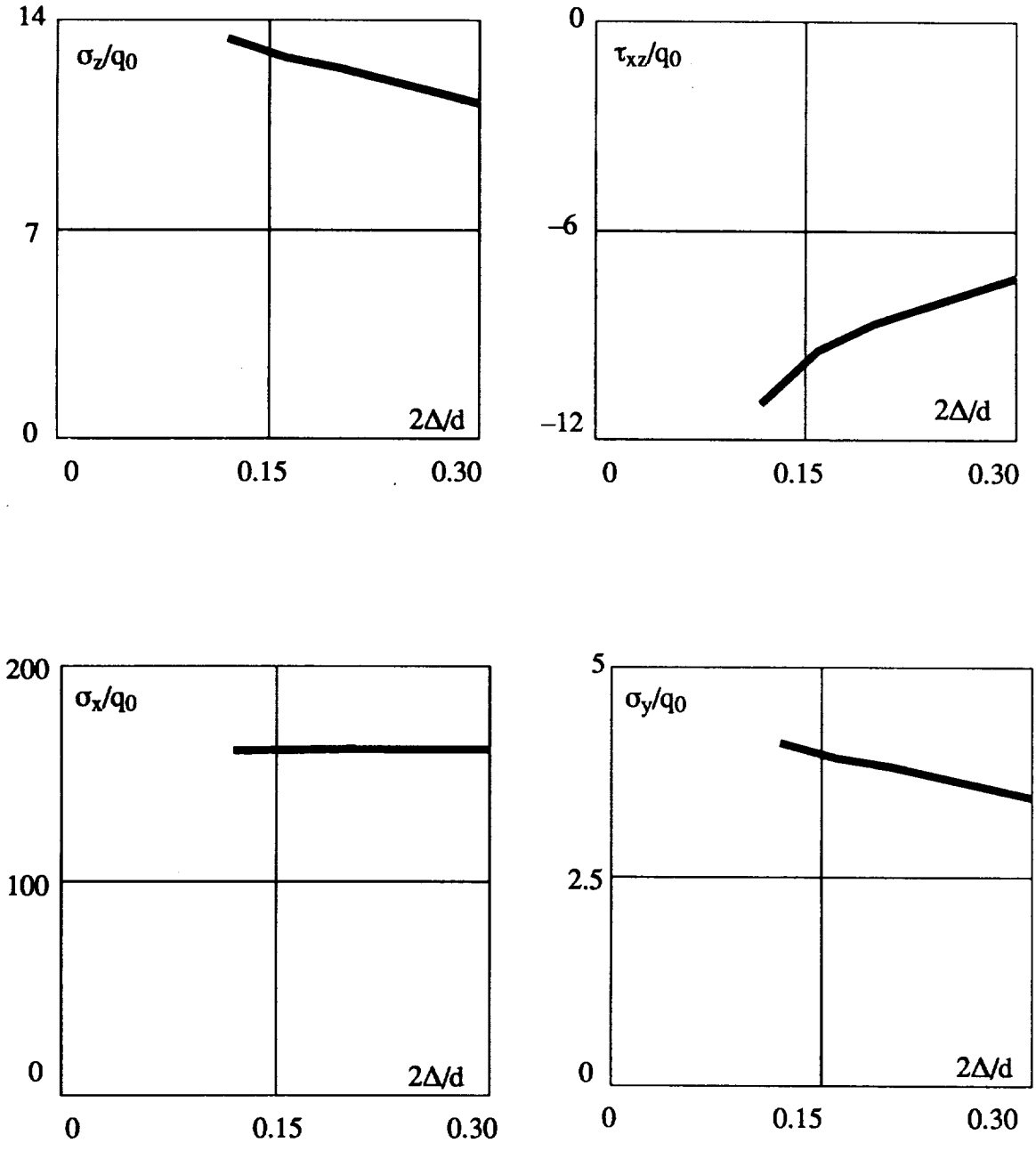

Figure 16. Dependencies of the σ_z, τ_{xz}, σ_x, and σ_y values at x=0.45a, y=0.5b, z=h_s on the mesh step Δ in x–direction.

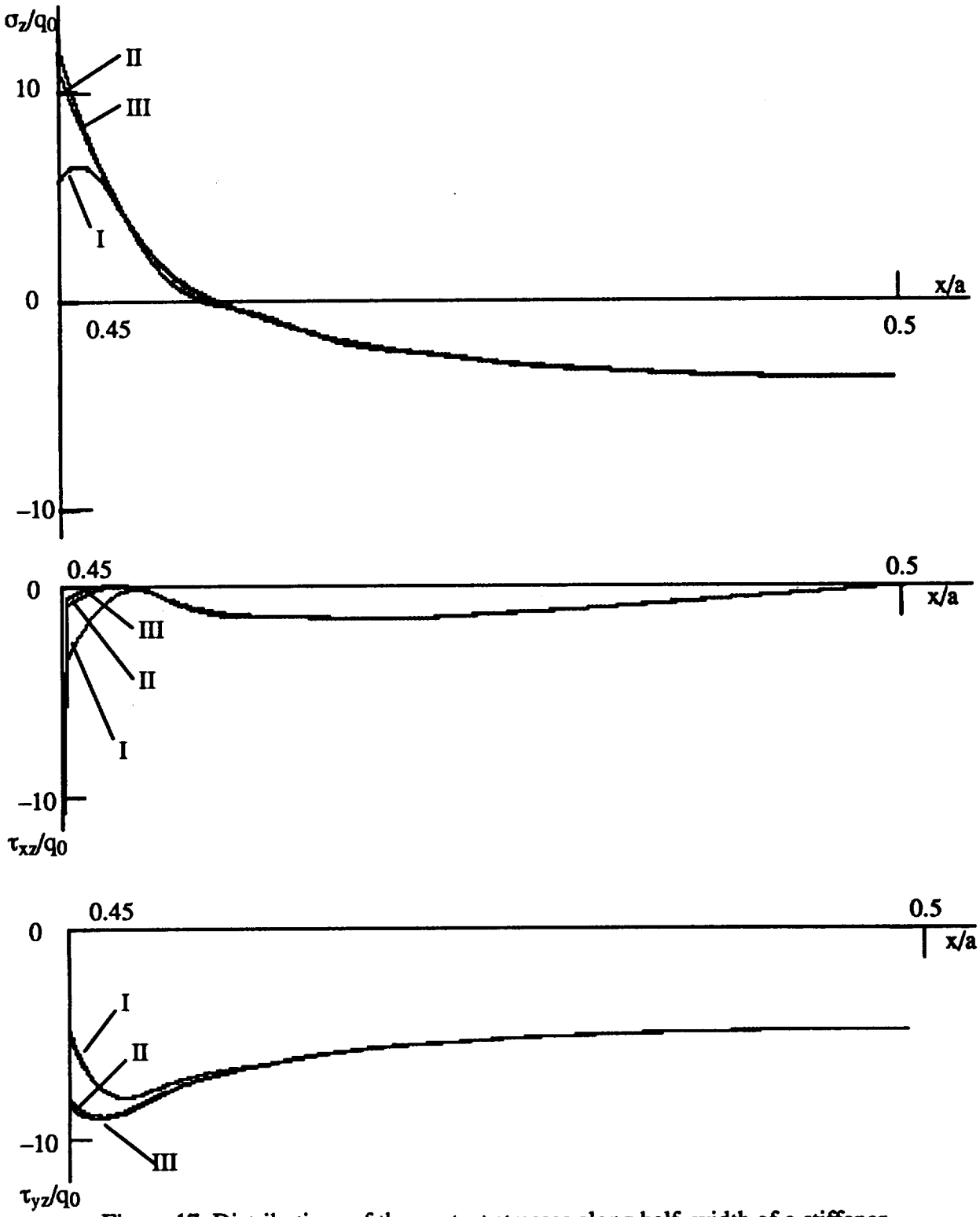

Figure 17. Distributions of the contact stresses along half–width of a stiffener for the divisions I, II, and III.

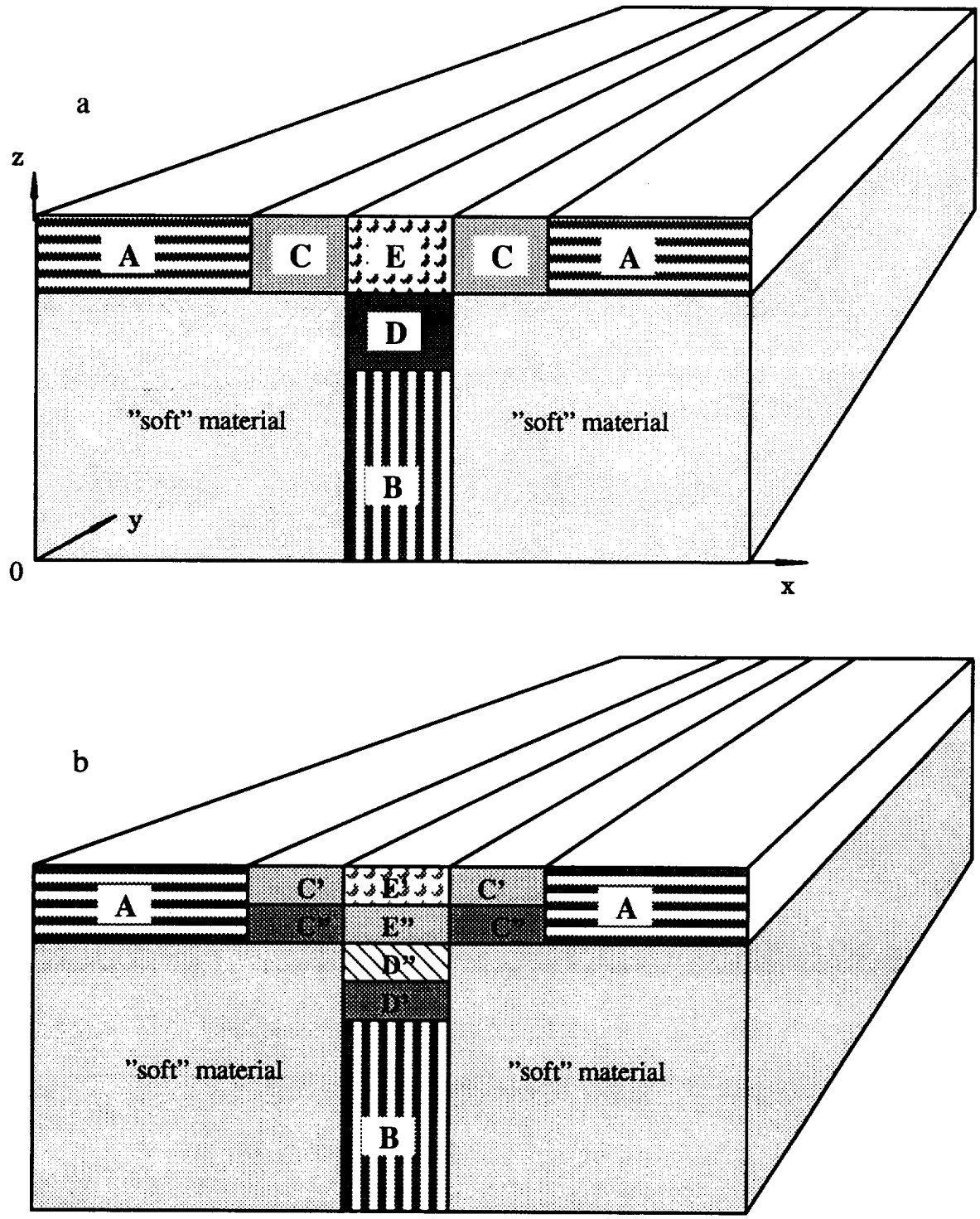

Figure 18. Meso–volume modelling of T–section triaxially braided plate.

Figure 19. Variation of σ_z along z coordinate at x=0.5a, y=0.5b.

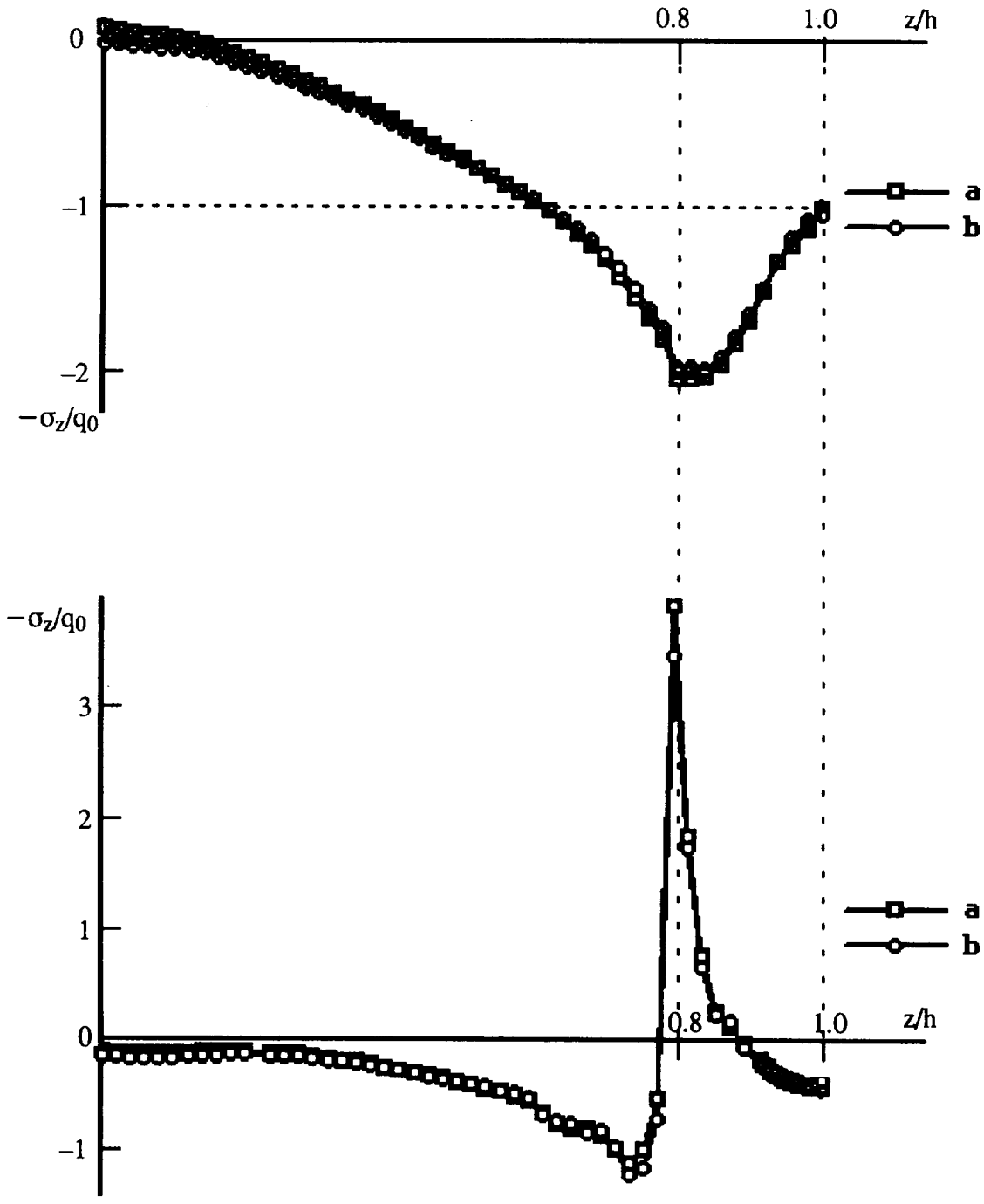

Figure 20. Variation of σ_z along z coordinate at x=0.4a, y=0.5b.

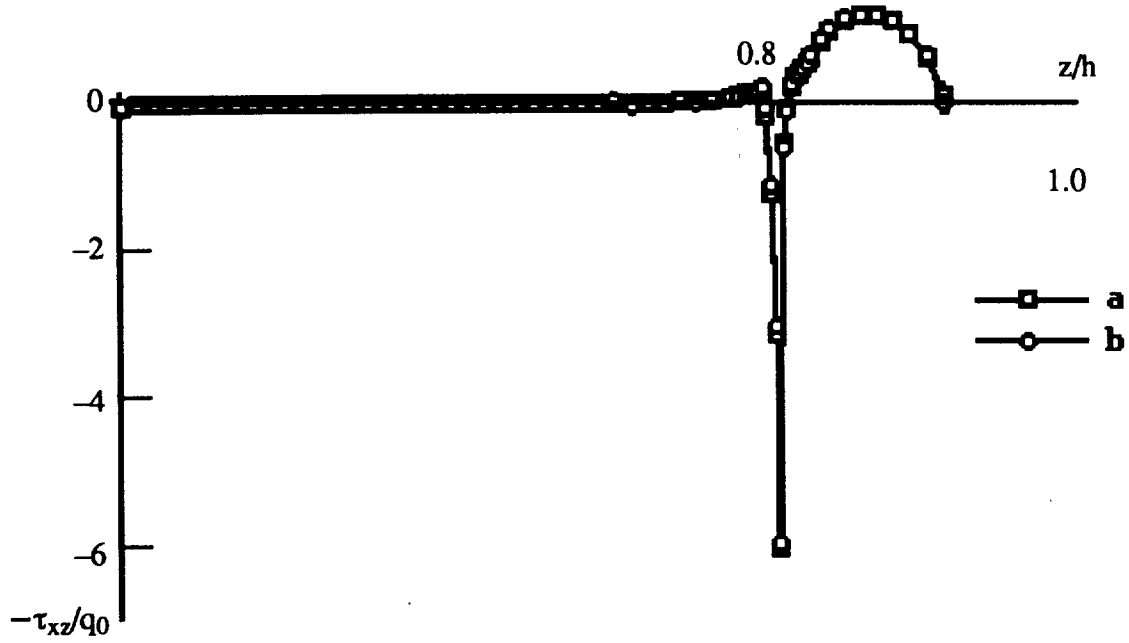

Figure 21. Variation of τ_{xz} along z coordinate at x=0.4a, y=0.5b.

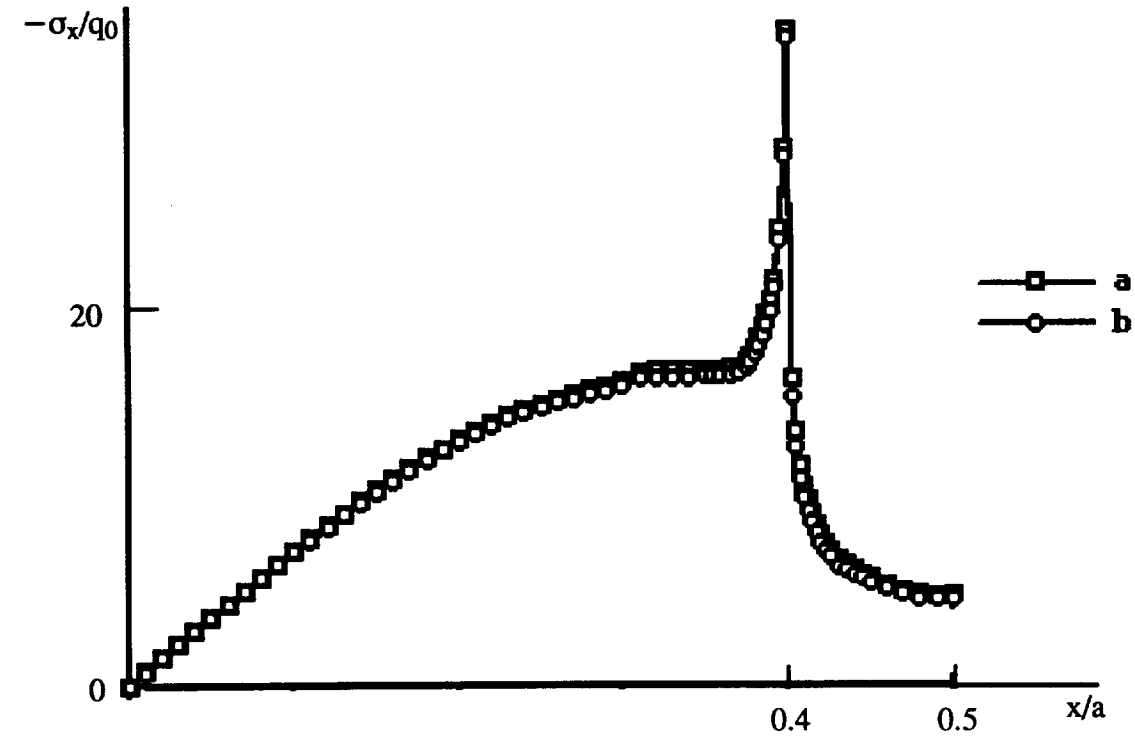

Figure 22. Variation of σ_x along x coordinate at y=0.5b, z=0.8h.

Figure 23. Variation of σ_z along x coordinate at y=0.5b, z=0.8h.

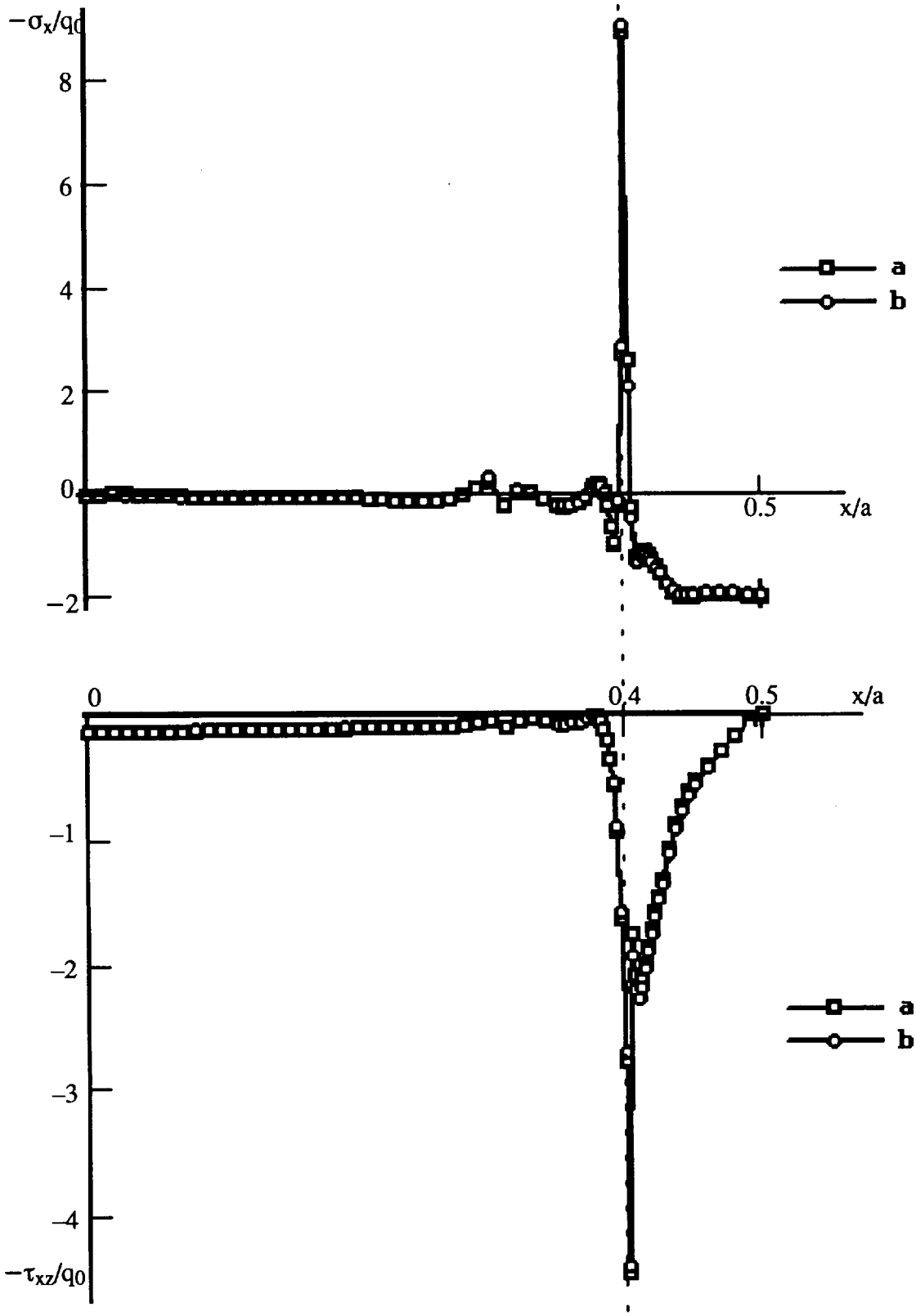

Figure 24. Variation of τ_{xz} along x coordinate at y=0.5b, z=0.8h.

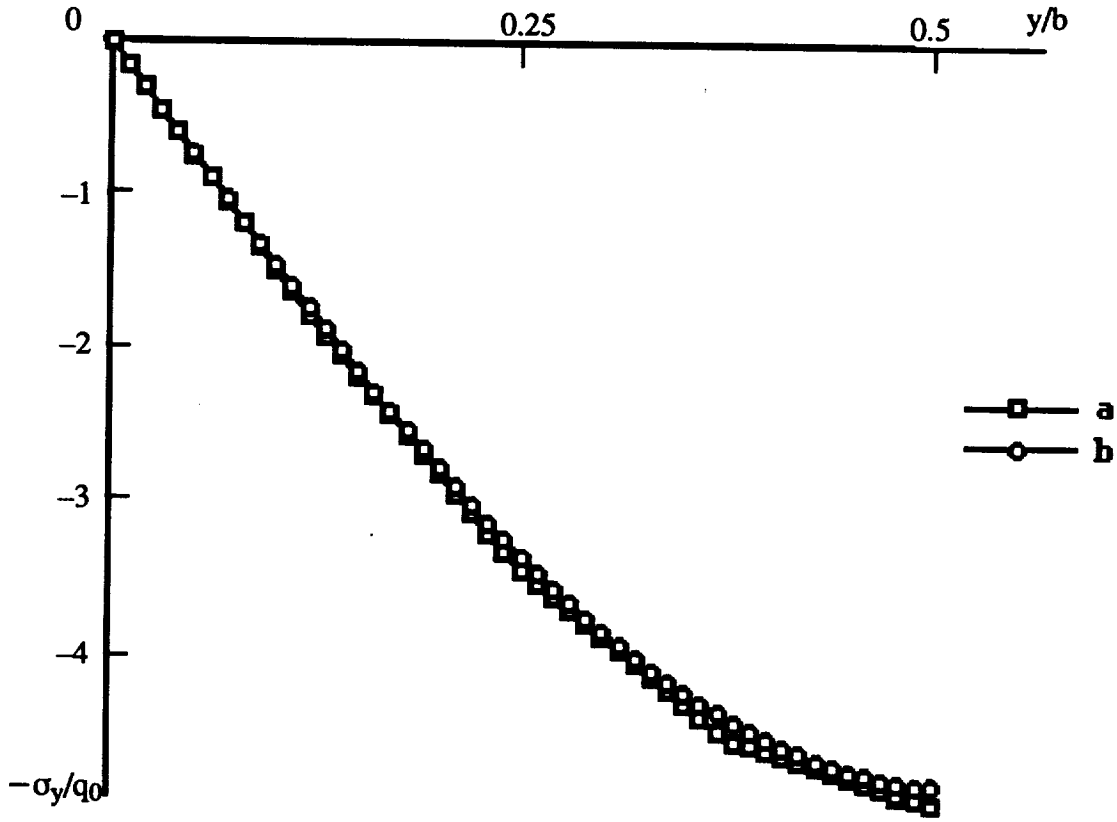

Figure 25. Variation of σ_y along y coordinate at x=0.5a, z=0.9h.

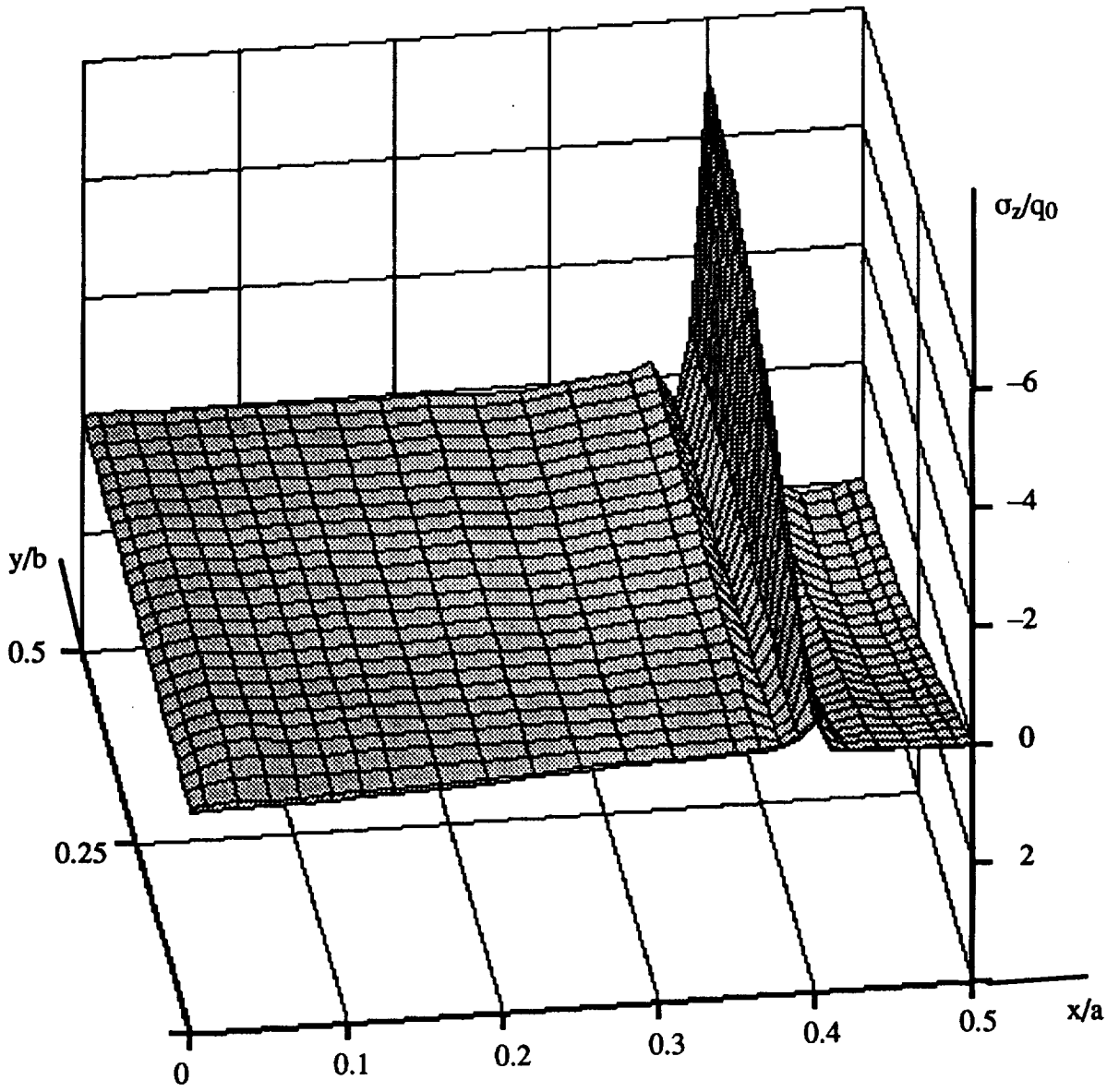

Figure 26. σ_z field in the plane z=0.8h.

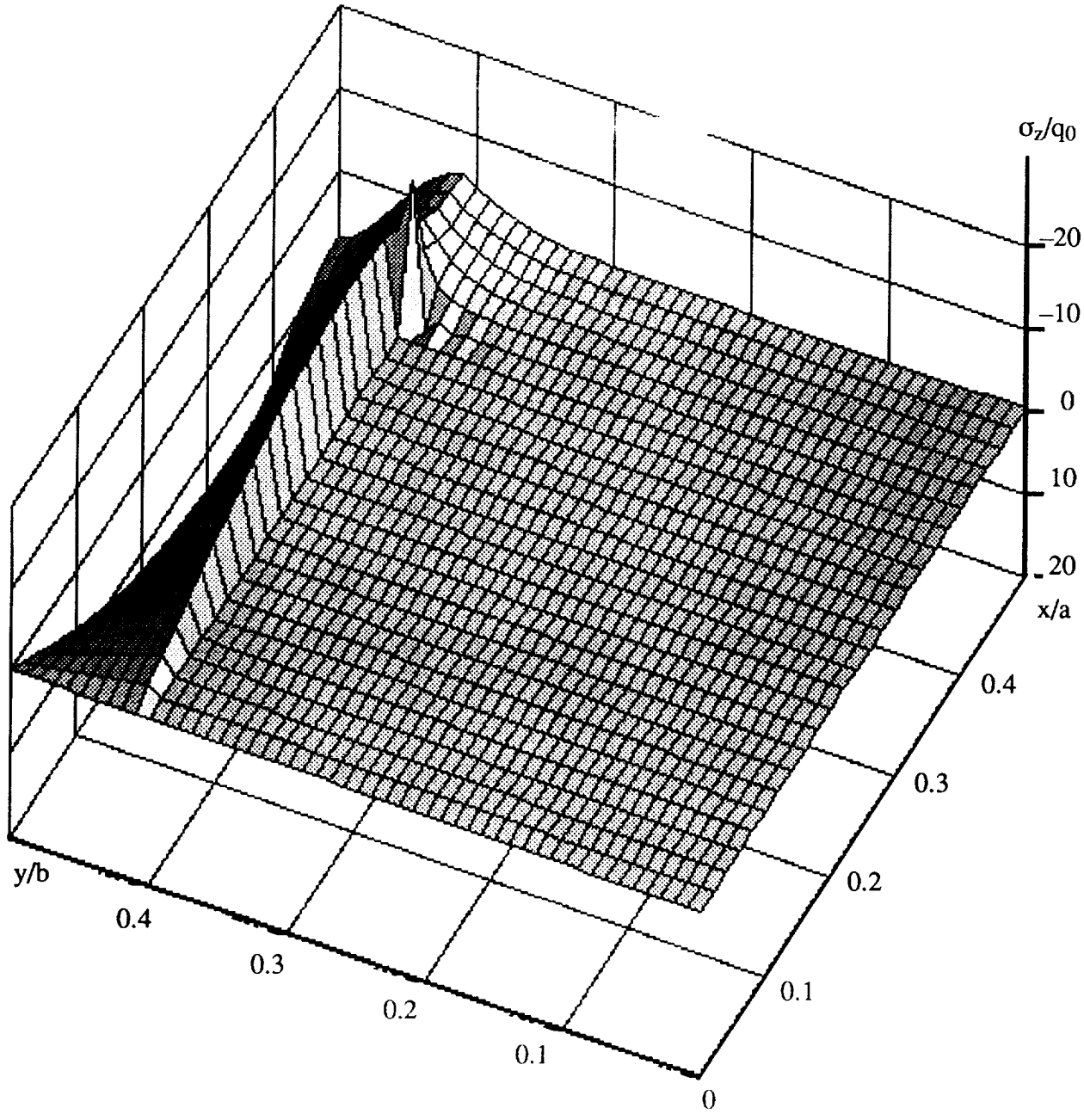

Figure 27. σ_x field in the plane z=0.8h.